Protein-lipid interaction at low pH induces oligomerisation of the MakA cytotoxin from *Vibrio cholerae*

Aftab Nadeem[1,2,3]*, Alexandra Berg[1,2,3,4], Hudson Pace[2,5,6], Athar Alam[2,3,5], Eric

Toh[1,2,3], Jörgen Ådén[2,7], Nikola Zlatkov[1,2,3], Si Lhyam Myint[1,2,3], Karina Persson[2,7],

Gerhard Gröbner[2,7], Anders Sjöstedt[2,3,5], Marta Bally[2,5,6], Jonas Barandun[1,2,3,4], Bernt

Eric Uhlin[1,2,3]*, Sun Nyunt Wai[1,2,3]*

[1]Department of Molecular Biology, Umeå University, SE-90187 Umeå, Sweden.

[2]Umeå Centre for Microbial Research (UCMR), Umeå University, SE-90187 Umeå, Sweden.

[3]The Laboratory for Molecular Infection Medicine Sweden (MIMS), Umeå University, SE-90187 Umeå, Sweden.

[4]Science for Life Laboratory (SciLifeLab), Department of Molecular Biology, Umeå University, SE-90187 Umeå, Sweden

[5]Department of Clinical Microbiology, Umeå University, SE-90185, Umeå, Sweden.

[6]Wallenberg Centre for Molecular Medicine, Umeå University, SE-90185, Umeå, Sweden.

[7]Department of Chemistry, University of Umeå, SE-901 87, Umeå, Sweden

Corresponding authors: Aftab Nadeem, e-mail: aftab.nadeem@umu.se

Bernt Eric Uhlin, e-mail: bernt.eric.uhlin@umu.se

Sun Nyunt Wai, e-mail: sun.nyunt.wai@umu.se

Short title: pH-dependent cytolytic MakA activity

Abstract (150 words)

Many pathogenic bacteria produce protein toxins that target and perturb host cell membranes. The secreted α-pore-forming toxins (α-PFTs) cause membrane damage via pore formation. This study demonstrates a remarkable, hitherto unknown mechanism by an α-PFT protein from *Vibrio cholerae*. As part of the MakA/B/E tripartite toxin, MakA is involved in membrane pore formation similar to other α-PFTs. In contrast, MakA protein alone induces tube-like structures in the acidic lysosomal host cell compartment. *In vitro* studies unravel the dynamics of tubular growth, which occur in a pH-, lipid- and concentration-dependent manner. A 3.7-Å cryo-electron microscopy structure of MakA filaments reveals a unique protein-lipid superstructure. In its active α-PFT conformation, MakA embeds its transmembrane helices into a thin annular lipid bilayer and spirals around a central cavity. Our study provides molecular insights into a novel tubulation mechanism of an α-PFT protein, revealing a new mode of action by a secreted bacterial toxin.

Introduction

Several bacterial protein toxins are known to interact directly with target cell membranes by binding specific receptors, lipids or proteins on host cell membranes[1,2]. Both extracellular and intracellular bacterial pathogens produce and secrete host membrane-attacking pore-forming toxins (PFTs) to counteract host defenses, to promote colonization and spread, and to kill other bacteria[3,4]. PFTs can be categorized into two main groups, α-PFTs and β-PFTs, based on whether the secondary structure of the membrane-penetrating domain contains α-helices or β-barrels, respectively[3]. Generally, PFTs are secreted from bacteria in a monomeric, soluble form. Upon recognition and binding to the target cell membrane, the toxins undergo a conformational change, interact with the membrane, dimerize, and oligomerize, leading to the formation of membrane pores[5].

Vibrio cholerae, a Gram-negative bacterium, is the causal organism of the diarrheal disease cholera[6]. Cholera toxin (CT) and toxin co-regulated pilus (TCP) are the main virulence factors of *V. cholerae* that cause disease in mammalian hosts[7,8]. Most

66   environmental *V. cholerae* isolates do not produce CT and TCP[9]. Nevertheless, these

67   bacteria are considered pathogenic since they have been associated with secretory

68   diarrhea and may cause wound infections and sepsis[10]. *V. cholerae* strains lacking the

69   cholera toxin-encoding genes often contain a set of genes coding for other secreted

70   virulence factors, including hemolysin, hemagglutinin protease, RTX toxin, and

71   multiple lipases that jointly may play a role in pathogenesis[10].

72

73   Using *Caenorhabditis elegans* and *Danio rerio* (zebrafish) as host models for bacterial

74   predatory interactions and infection in aqueous environments, respectively, we

75   obtained evidence for a new *V. cholerae* cytotoxin denoted MakA (motility-associated

76   killing factor A)[11]. The *V. cholerae* gene *makA* (*vca0883)* is localized in a gene cluster

77   together with *makC* (*vca0881*), *makD* (*vca0880), makB* (*vca0882*) and *makE*

78   (*vca0884*). This gene cluster has been found in different *V. cholerae* strains, including

79   CT-negative isolates[11,12,13]. The crystal structure of MakA revealed that it belongs to

80   the ClyA α-PFT family[11], named after the potent, one-component, pore-forming toxin

81   ClyA which is expressed from a monocistronic operon in *E. coli*[14,15]. Our recent studies

82   of the proteins encoded by the *mak* genes in *V. cholerae* demonstrated that MakA can

83   form a tripartite cytolytic complex with MakB and MakE, whereas neither of the three

84   proteins display cytolytic activity on their own[13]. Other family members of α-PFT are

85   found among the bipartite toxins from *Yersinia enterocolitica* (YaxAB)[16,17] and

86   *Xenorhabdus nematophila* (XaxAB)[17], as well as among the tripartite toxins from

87   *Bacillus cereus* (NheABC and HblL$_1$L$_2$B)[18], *Aeromonas hydrophila* (AhlABC)[19] and

88   *Serratia marcescens* (SmhABC)[20]. The bipartite and tripartite PFTs require the

89   combined action of all protein partners to induce pore formation in the target

90   membranes, and there is evidence that protein interactions occurs in a specific order

91   for maximum cytolytic activity[19,20,13]. However, there are still questions about how many

92   molecules of each subunit protein are required to form a pore, how they interact with

93   each other, how structural conformational changes occur, and how protein moieties

94   are involved in the interaction with the host membrane. In addition, it remains possible

95   that some of the subunit proteins can be separately released from the bacteria and

96   thereby exhibit biological effects on their own. Secretion of the MakA/B/E proteins from

97   *V. cholerae* was shown to be facilitated via the bacterial flagellum[11,13]. However, about

98   10% of MakA was secreted from *V. cholerae* lacking the flagellum suggesting an

3

99 alternative route of secretion, in contrast to MakB and MakE, which displayed a more

100 definitive flagellum-dependent secretion[11,13].

101

102 Our earlier studies with MakA and cultured mammalian cells showed that the protein

103 binds to the target cell membrane and, upon internalization, may accumulate in the

104 endolysosomal membrane, causing lysosomal dysfunction, induction of autophagy

105 and apoptotic cell death[21,22]. Moreover, MakA can modulate host cell autophagy in a

106 pH-dependent manner[23].

107

108 The present study aimed to further characterize the mechanism(s) behind MakA-

109 induced lysosomal membrane tubulation and the pH-dependent molecular

110 interaction(s) between MakA and host cell membranes. We found that under low pH

111 conditions, MakA bound to purified lysosomes and to liposomes prepared from total

112 epithelial cell lipid extracts (ECLE). The insertion of MakA into lysosomes and ECLE

113 liposomes resulted in the formation of tubular assemblies. Cryo-electron microscopy

114 (cryo-EM) analysis of these assemblies revealed an unusual helical structure formed

115 by MakA and lipid spirals. The observed structure revealed that MakA monomers

116 adopted conformational arrangements typical of active membrane-bound α-PFTs while

117 they assembled into an atypical polymeric superstructure. Large structural

118 rearrangements, presumably induced by the lowered pH, were necessary for the

119 transition from the inactive soluble form to the extended active toxin form. Interaction

120 of these MakA structures with cell membranes could lead to cell death in the *in vitro*

121 setting. MakA is the first *V. cholerae* protein that engages target membranes to form

122 nanotubes by polymerizing as a helical structure together with a lipid spiral.

123

Results

pH-dependent formation of tubular structures in lysosomes and on cell membranes by MakA

127 In recent *in vitro* studies with epithelial cells, we found that internalized MakA protein

128 accumulated in the acidic endolysosomal compartment where it caused formation of

129 tube-like structures and induced lysosomal permeability[22]. Our findings prompted us

130 to examine how the observed lysosomal tubulation and lysosomal dysfunction might

131 be caused by MakA. Upon treatment of Caco-2 cells with MakA (250 nM, 18 h), we

132 observed co-localization of the Alexa568-labeled MakA (Alexa568-MakA) with GFP-
133 LAMP1 or lysotracker in tubular structures (**Fig. 1a and Supplementary Fig. 1a**). The
134 tubulation in the lysosomes was further confirmed by transmission electron microscopy
135 (TEM) of lysosomes isolated from MakA-treated HCT8 cells (**Fig. 1b**). To investigate
136 if MakA can also induce tubulation of lysosomes outside the intracellular environment,
137 we purified lysosomes from untreated HCT8 cells and exposed them to native MakA
138 or to Alexa568-MakA. Both confocal microscopy and TEM analysis revealed
139 aggregation and tubulation of lysosomes at pH 5.0 (**Fig. 1c-d**). In addition, a majority
140 of the lysosomes showed well-organized tubulation when exposed to MakA at pH 6.5
141 (**Fig. 1d**). In contrast, we did not observe any MakA-induced tubular structures in
142 lysosomes at pH 7.0 (**Fig. 1d**). Western blot analysis confirmed pH-dependent binding
143 of MakA to lysosomes (**Fig. 1e**). Alexa568-MakA was subsequently shown to bind
144 epithelial cells in a pH-dependent manner (**Fig. 1f-g**). To determine the kinetics of
145 MakA binding to the target cells, HCT8 cells were exposed to Alexa568-MakA at pH
146 5.0, and live-cell imaging was performed using spinning disc confocal microscopic
147 analysis. Consistent with our earlier findings[21], we observed accumulation of
148 Alexa568-MakA on the plasma membrane, including filipodia-rich tubular structures, in
149 a time-dependent manner (**Fig. 1h and Supplementary Fig. 1b-c**). The time scale of
150 MakA binding to individual HCT8 cells ranged from ~40 minutes to 4 hours after
151 Alexa568-MakA treatment (**Fig. 1f-h and Supplementary Fig. 1b-c**). Ultimately,
152 Alexa568-MakA was detected on the plasma membrane of the entire cell population,
153 with most cells positive for tubular structures protruding out from the plasma membrane
154 (**Fig. 1f and 1h**). Taken together, these results suggest that MakA can cause tubulation
155 of both endolysosomal membranes and plasma membranes in a pH-dependent
156 manner.

pH-dependent epithelial cell toxicity and formation of tubular structures on erythrocytes by MakA

160 To further assess the effect of pH on the binding of MakA to HCT8 epithelial cells, we
161 performed Western blot analysis using anti-MakA antiserum (**Fig. 2a**). We observed
162 that MakA bound to the cells in a pH-dependent manner, and moreover, that there
163 seemed to be a pH-dependent formation of stable MakA oligomers bound to the
164 epithelial cells. To determine if MakA binding and oligomerization at the target cell
165 membrane correlated with cytotoxic effect, HCT8 cells were exposed to MakA, and cell

166   toxicity was quantified by a propidium iodide uptake assay using flow cytometry and

167   fluorescence microscopy (**Fig. 2b and Supplementary Fig. 2a**). In addition to causing

168   pH-dependent toxicity of HCT8 cells, MakA was similarly toxic to other colon cancer

169   cells, Caco-2 and HCT116 cells, as assessed by the MTS cell viability assay

170   (**Supplementary Fig. 2b**).

171

172   Erythrocytes are widely used as a cell model to investigate the cytolytic activity of the

173   toxins that belong to the ClyA pore-forming toxins family[14,17,18,24,25]. To test if pH-

174   dependent binding and oligomerization of MakA may cause hemolysis of erythrocytes,

175   human erythrocytes were exposed to increasing concentrations of MakA at different

176   pH conditions for either 90 min or 5 h (**Fig. 2c**). When erythrocytes were exposed to

177   MakA at pH 5.0, hemolysis was observed in a concentration dependent manner within

178   90 min (**Fig. 2c**). In contrast, MakA failed to induce hemolysis of erythrocytes at pH 6.5

179   or pH 7.4 during the 90 min treatment. A detectable, but low level of hemolysis was

180   observed after 5 h with erythrocytes exposed to MakA at pH 6.5 (**Fig. 2c**). With

181   confocal microscopy, we observed pH-dependent binding of Alexa568-MakA to

182   erythrocytes. A majority of erythrocytes at pH 5.0 and 6.5 were covered by Alexa568-

183   MakA whereas there was virtually no MakA binding observed at pH 7.4 (**Fig. 2d and**

184   **Supplementary Fig. 2c**). Notably, we detected the presence of tubular structures in

185   association with MakA at the red blood cell surface, as shown by a maximum 3D

186   projection of the z-stack images of erythrocytes (**Fig. 2e**). The presence of MakA-

187   induced tubular structures on the surface of erythrocytes was further observed by TEM

188   and scanning electron microscopy (SEM) (**Fig. 2f-g**). Together, these results suggest

189   that MakA could accumulate in a pH-dependent manner at the surface of both epithelial

190   cells and erythrocytes, thereby inducing formation of tubular structures that ultimately

191   might lead to cell lysis.

192

193   **MakA induction of tubular structures on liposomes lacking other proteins**

194   To investigate if tubulation of host membranes in response to MakA would require a

195   specific membrane protein or receptor, we created protein- and cytosol-free liposomes

196   using an epithelial cell total lipid extract (ECLE) isolated from HCT8 cells. After addition

197   of MakA, the liposomes were pelleted by centrifugation and the presence of MakA in

198   either the pellet or the supernatant was detected by Western blot analysis

199   (**Supplementary Fig. 3a**). The results indicated that more MakA was associated with

200   the liposomes at pH 5.0 and 6.5 than at pH 7.4. The interaction between MakA and

201   ECLE liposomes at pH 6.5 was quantified by surface plasmon resonance (SPR)

202   analysis (**Fig. 3a**). MakA displayed significant interaction with ECLE liposomes, with

203   an estimated K_D of 49.2 nM. Importantly, MakA at the highest tested concentration

204   (200 nM) failed to interact with the liposomes prepared from zwitterionic 1-palmitoyl-2-

205   oleoyl-sn-glycero-3-phosphocholine (POPC), used as a negative control (**Fig. 3a**).

206

207   To determine the effect of pH on MakA's conformational properties, the protein was

208   subjected to circular dichroism (CD) spectroscopy analysis at different pH in the

209   absence or presence of ECLE liposomes (**Fig. 3b-c**). In the absence of liposomes, the

210   CD spectra indicated a decrease in the α-helical content of the protein when in the

211   acidic environment. This decrease in α-helical content of MakA was restored when

212   ECLE liposomes were present, suggesting that liposomes somehow stabilized the

213   structure of MakA (**Fig. 3b-c and Supplementary Table 1**). TEM analysis of MakA at

214   different pH indicated that it formed oligomeric structures in a pH-dependent manner

215   (**Supplementary Fig. 3b**).

216

217   Further examination by TEM addressed if there were morphological changes in the

218   ECLE liposomes upon exposure to increasing concentrations of MakA at pH 6.5 (**Fig.**

219   **3d and Supplementary Fig. 3c**). Similar to the tubulation observed for the target cell

220   membranes and lysosomes, MakA triggered tubulation of the ECLE liposomes in a

221   concentration-dependent manner (**Supplementary Fig. 3c**). Concomitant with the

222   assembly of tubular structures emanating from the liposomes, the size of the liposomes

223   appeared to shrink as the tubules grew up to several micrometers in length. Ultimately,

224   the entire liposome seemed to be transformed into long tubules (**Fig. 3h and**

225   **Supplementary Fig. 3c-e**). The tubulation of ECLE liposomes was also observed by

226   confocal microscopy upon treatment with Alexa568-labeled MakA (**Supplementary**

227   **Fig. 3d-e**). In the same population of small liposome particles, we also detected

228   Alexa568-MakA-positive large lipid vesicles (5-10 μm in size, less than 1% of the entire

229   liposome fraction). The z-stack projection suggested that the whole lipid vesicle was

230   decorated with a bundle of fluctuating tubules (**Supplementary Fig. 3e**). To further

231   assess whether or not any protein or glycolipid receptor mediated the observed

232   membrane tubulation by MakA, liposomes were prepared from a well-defined synthetic

233   lipid mixture (SLM); whose composition was inspired by the distribution of lipids found

234   in the plasma membrane of HeLa cells[26]. Tubulation of the SLM liposomes by MakA

235   was observed by TEM (**Fig. 3d**). In addition to the tubular structures, we observed a

236   large number of well-organized, star-shaped oligomeric particles of MakA among the

237   ECLE liposomes (**Supplementary Fig. 3c**). Furthermore, the presence of MakA

238   protein in the tubular structures was evidenced by immunogold staining using MakA-

239   specific antibodies (**Fig. 3e**). By fluorescence microscopy we were able to visualize

240   tube growth originating from a supported lipid bilayer (SLB) prepared from SLM

241   liposomes containing the fluorescent lipid Texas Red-DHPE, demonstrating that the

242   tubes also contain lipids from the SLB (**Fig. 3f and Movie 1**).

243

244   We next investigated the kinetics of MakA protein-lipid tubulation. Using fluorescence

245   microscopy, we found that administering Alexa568-MakA to a SLB prepared from SLM

246   liposomes prompted a significant and highly dynamic membrane remodeling (**Fig. 3g**

247   **and Movie 2**). Within 10 minutes, Alexa568-MakA binding to the SLBs resulted in

248   formation of MakA-associated tubules of various sizes (**Fig. 3g**). Based on these

249   findings, we propose a schematic model for how the MakA-liposome interaction can

250   result in the formation of the observed protein-lipid tubular structures (**Fig. 3h**). At pH

251   6.5 or lower, MakA may adopt a conformation that allows the protein to insert into the

252   lipid membrane in the form of an oligomer assembly that can start to spiral around the

253   lipids of the membrane leading to formation of a growing tube structure. Concomitantly

254   the size of the vesicle appear to shrink, and the tube may grow up to several

255   micrometers in length. Our results suggest that the MakA-lipid tubulation can occur

256   without the involvement of other proteins or some specific protein receptor under the

257   pH conditions tested.

258

259   **Structure of the MakA filament**

260   We used helical reconstruction to solve the cryo-EM structure of a MakA filament

261   assembled *in vitro* in the presence of ECLE liposomes at pH 6.5 and high protein

262   concentrations (**Fig. 4a and Supplementary Fig. 4**). An initial 2D classification

263   allowed us to identify repetitive elements and measure a helical repeat distance of

264   ~216 Å (**Fig. 4b and Supplementary Fig. 5a**). A subsequent investigation of the layer

265   line distances in a collapsed power spectrum of selected well-resolved class averages

266   confirmed this distance (**Supplementary Fig. 5b**). Next, we performed a preliminary

267   3D refinement of filament segments from well-defined 2D class averages without

8

268 imposing symmetry (**Supplementary Fig. 4**). This volume was visually inspected to

269 deduce the helical symmetry parameters (**Supplementary Fig. 5c-d**). One repeating

270 element of the right-handed spiral consists of 37 tetramers that complete five turns

271 around the helical axis, spanning a length of 216.5 Å and a diameter of 322 Å. This

272 arrangement results in an axial rise of 5.85 Å per subunit and a helical twist of 48.65˚

273 (**Fig. 4b and Supplementary Fig. 5d**). Application of these initially calculated values

274 with local searches in a 3D refinement further optimized symmetry parameters,

275 resulted in a cryo-EM map at an overall resolution of 3.7 Å (**Supplementary Table 1**

276 **and Supplementary Fig. 6**). The obtained cryo-EM map features a well-resolved

277 central transmembrane helix (TMH) region and a less well-resolved peripheral region

278 (**Fig. 4c**). We isolated two MakA tetramers from the segments using signal subtraction

279 and subjected the resulting particles to 3D classification and refinement to improve the

280 peripheral density and connectivity. The clear connectivity of the obtained density map

281 (**Fig. 4d and Supplementary Fig. 6e**) allowed for reliable secondary structure

282 placement using the MakA soluble state crystal structure (PDB-6EZV[11]). High-

283 resolution features in the helical reconstruction (**Fig. 4c and Supplementary Fig. 6f**)

284 allowed for *de novo* model building of structural elements in the central region.

285 However, due to continuous rotation along the filament axis, flexibility (**Supplementary**

286 **Fig. 4**), and the conformational difference with respect to the crystal structure, the

287 MakA tail domain structure is less reliable and modeled with poly-alanine secondary

288 structure elements.

289

290 MakA oligomerizes into a filamentous structure growing from or ending in membranous

291 vesicles (**Fig. 4a, Supplementary Fig. 4**). The building blocks of this filament are

292 formed by two MakA dimers (**Fig. 4b and 4d**) that organize into a pinecone-like

293 architecture, spiraling around a central cavity (**Fig. 4c**). From the top view along the

294 filament axis, the helix features a propeller-like structure with a weak, annular density

295 embedded in between the blades formed by MakA (**Fig. 4c**). This density resembles

296 lipid tails and contains some spherical features, which could be associated with

297 phospholipid heads, suggesting the presence of a thin phospholipid bilayer that spirals

298 around the central cavity of the filament (**Fig. 4c**). Interestingly, the annular density is

299 located between the transmembrane helices of MakA (**Fig. 4d**), indicating that the

300 active toxin form interacts with lipid vesicles and starts to oligomerize by internalizing

301 membrane lipids.

302

A significant conformational change is required to adopt the membrane-bound state

The basic building block of the observed protein-lipid filament is formed by four MakA subunits in a membrane-bound active conformation (**Fig. 5a,b**). This conformation of MakA is significantly different from the previously reported soluble state structures resembling the inactive form (PDB-6DFP and PDB-6EZV[11]). In the soluble form, a C-terminal tail (res. 351-365, **Fig. 5c**, purple) inactivates the predicted transmembrane domains by forming a β-tongue, consisting of three β-sheets[11], that shields the hydrophobic residues from the surrounding solvent. This shielding characteristic is well-described for the soluble form of the ClyA pore-forming toxin family, including ClyA, Hbl-B, NheA, and AhlB[17,19,27-30]. MakA undergoes a structural change comparable to the opening of a Swiss army knife blade when it shifts from a soluble inactive to a membrane-bound active state, where the helix bundle of the tail region represents the handle, the transition from the tail to the neck region forms two hinges, and the β-tongue together with 4 and 5 resembles the blade that folds out (**Fig. 5c**, α4 & α5; light & dark green). Additionally, the β-tongue changes its secondary structure and, together with α4 and α5/α6, forms two extended helices (**Fig. 5c**). This significant conformational change leads to the formation of two TMHs and a short loop region (res. 219-221) between α4 and α5. Interestingly, despite certain similarities, all four copies of MakA adopt different conformations within the tetramer, indicated by MakA-1 to MakA-4 (**Fig. 4 and Fig. 5**). The most significant structural differences between the four MakA conformations can be observed in the neck and head domains, connected via a hinge with the tail domains (**Fig. 5c**). The hinge allows for different degrees of bending (opening up of the Swiss army knife), while the neck helices α4 and α5 and the loop region (res. 219-221) display a high degree of plasticity. For the peripheral tail domain, two major conformations can be observed. In MakA-2 and MakA-4, this region superimposes well with the crystal structure, whereas helix α6 of MakA-1 and MakA-3 moves by almost 10 Å to extend the length of α5. While the N-terminal helices of the stretched MakA states are reduced compared to those of the kinked MakA forms, the C-terminal β-strand (res. 351-365), covering the TMH in the soluble state, is disordered in all four subunits.

334

335

Discussion

Recent studies have revealed how different bacterial species, notably *B. cereus*, *A. hydrophila*, *S. marcescens* and *V. cholerae*, have the capability to produce structurally similar tripartite protein complexes that assemble on host cell membranes as pore structures that are cytolytic[13,18-20]. In the case of *V. cholerae,* it has become evident that the MakA component of the tripartite complex, when presented alone to mammalian cells, is effectively internalized and accumulates on endolysosomal membranes, leading to induction of autophagy and apoptotic cell death[21-23]. Herein, we show that MakA is able to produce a novel protein-lipid polymeric superstructure at low pH (6.5 or below) that perturbs host cell membranes.

Several prokaryotic proteins are known to polymerize in the presence of a matrix such as a lipid membrane or DNA. This type of assembly is referred to as a collaborative filament[31]. In the presence of lipid membranes, collaborative filaments are assembled by a bridging protein and lipid on the membrane in a sequence-specific manner and by sensing membrane curvature[31]. It was demonstrated that membrane-mediated clustering of Shiga toxin molecules and the formation of tubular membrane invaginations are essential steps in the clathrin-independent Shiga toxin uptake process[32]. In earlier studies, pH-dependent membrane insertion and increased cytotoxic activity were demonstrated for different bacterial toxins, including anthrax toxin from *Bacillus anthracis*[33], diphtheria toxin from *Corynebacterium diphtheriae*[30], VacA from *Helicobacter pylori*[33]*,* perfringolysin from *Clostridium perfringens*[34], and listeriolysin O from *Listeria monocytogenes*[35]. Recent research on the pre- and pore forms of mammalian pore-forming toxin, mammalian perforin 2 (mPFN2), provide interesting insights into the pore generation process. It was demonstrated that pre-pore-to-pore transformation occurs at an acidic pH, which is accomplished by a 180° rotation of the membrane attacking domain and β-hairpin P2 domains with respect to one another, allowing membrane insertion to take place[34]. Similar to these other toxins, a decrease in pH facilitated the MakA structural change comparable to the opening of a Swiss army knife blade when shifting from a soluble to a membrane-bound active state interaction with the lipid membrane. The pH-induced structural change potentiated the MakA-induced cytotoxic effect on the target cell under the conditions tested. Consistent with these results, we recently found that MakA co-localizes with β-

11

369 catenin, actin and the phosphatidic acid biosensor, PASS, in filipodia-rich
370 structures[21,22].

371

372 Our *in vitro* analysis of the low-pH-induced interaction between MakA and host
373 membranes included: purified lysosomes, cultured epithelial cells, red blood cells, and
374 liposome models. In all model systems, we observed that low pH enhanced the activity
375 of MakA, characterized by a striking tubulation of both purified lysosomes and
376 liposomes prepared from epithelial cell total lipid extract. Furthermore, it was found
377 that MakA formed tubular structures on liposomes independent of any specific protein
378 receptor or energy-generating molecules, i.e., ATP or GTP, suggesting that at low pH
379 the structural change and insertion of MakA itself was sufficient to trigger tubulation at
380 the membrane surface. In contrast to some other PFTs that need cholesterol for
381 oligomerization[35-37], MakA could induce tubulation on liposomes obtained from lipid
382 sources essentially lacking cholesterol, *i.e. E. coli* and *C. elegans*, showing that the
383 pH-dependent tubulation of MakA can occur in the absence of cholesterol in the
384 membrane. Bacterial cell membranes are typically devoid of cholesterol[38], while the
385 membranes of *C. elegans* are mostly composed of glycerophospholipids and
386 sphingolipids, with trace quantities of cholesterol[39]. In addition, we observed that the
387 presence of cholesterol was not required for the oligomerization of MakA in solution
388 (**Supplementary Fig. 3b**).

389

390 Importantly, unlike Shiga toxin and cholera toxin, which insert into the membrane and
391 cause inward-directed tubulations of artificial lipid membranes since toxin binding
392 induces negative curvature of the plasma membrane[40-42], MakA evidently could drive
393 the rapid growth of tubules towards the extracellular space as shown with red blood
394 cells (**Fig. 2g**). We propose that the appearance of tubular structures in response to
395 MakA was a direct consequence of MakA insertion into the membrane, which
396 appeared to create the conditions for generating a positive curvature, as described
397 previously for protein-lipid complexes and multi-anchoring polymers[43,44].

398

399 Our findings allowed us to propose a model for MakA oligomer assembly and its
400 implications for pore formation. Within the oligomerized MakA filament, the TMHs line
401 the inner cavity, interacting with lipids, which are intercalated both within the dimer
402 interface and between the dimers in the helical spiral (**Fig. 4c and Fig. 5b**). In the

12

403   context of pore-forming toxin systems, the initial insertion of one toxin component was

404   described for XaxAB[17], YaxAB[16], and suggested for AhlC[19]. Considering that the TMHs

405   of the MakA-tetramers harbor a lipid bilayer, it could be assumed that MakA initiates

406   membrane insertion in a manner similar to its role in pore formation under neutral pH

407   conditions when part of the tripartite MakA/B/E complex[13]. We hypothesize that under

408   low-pH conditions, MakA transitions from inactive to the active stretched conformation

409   and penetrates the membrane as a monomer. In the membrane bound state, the

410   interaction of the head and tail domains of two monomers might lead to MakA dimer

411   formation and subsequent oligomerization.

412

413   The pronounced structural difference between two subunits forming a dimer, in the

414   absence of the tripartite complex interaction partner, i.e., MakB or MakE, would reflect

415   how MakA's plasticity nevertheless can structurally mimic the expected structure when

416   involved in the tripartite cytolysin. First, one completely stretched monomer dimerizes

417   with a monomer with a pronounced elbow-like kink from α3 to α4 in the transition from

418   the tail to the neck region (**Fig. 5c**). Subsequently, the two dimers form a tetramer with

419   the stretched and kinked MakA states associating with each other, respectively. The

420   subsequent tetramerization followed by oligomerization does not result in pore

421   formation, but helical growth and shearing off of lipids from vesicles and cell

422   membranes at low pH. This process, which does not occur in the tripartite cytotoxin

423   scenario under neutral pH conditions, depletes membranous structures of lipids and

424   potentially causes cell lysis in a manner quite different from that of a *bona fide* α-PFT

425   cytolysin complex. Our findings with the *V. cholerae* MakA protein reveal an

426   unexpected capability and remarkable mode of action of an individual α-PFT toxin

427   subunit.

428

Materials and Methods

Chemical and Lipids

431 Chloroform, formaldehyde, methanol, sodium citrate, Tween 20, Triton X-100 and

432 Fluoromount were from Sigma (St Louis, MO, USA). Hoechst 33342 and Lysotracker

433 were from Thermo Fisher Scientific (Waltham, MA, USA). Propidium iodide was from

434 BD Biosciences (San Jose, CA). Protease inhibitor and phosphatase inhibitor,

435 phosSTOP were from Roche (Roche AB, Solna, Sweden). All lipids were purchased

436 from Avanti Polar Lipids (Alabaster, AL, USA). Lipids: 1-palmitoyl-2-oleoyl-glycero-3-

437 phosphocholine (POPS), 1,2-dioleoyl-sn-glycero-3-phosphoethanolamine (DOPE), 1-

438 palmitoyl-2-oleoyl-sn-glycero-3-phospho-L-serine (POPS), Sphingomyelin from

439 Porcine Brain (SM), Cholesterol from Ovine (Chol), L-α-phosphatidylinositol-4,5-

440 bisphosphate from Porcine Brain (PIP2), and N-palmitoyl-sphingosine-1-

441 {succinyl[methoxy(polyethylene glycol)5000]} (PEG5Kce). Lyophilized PIP2 lipids

442 were dissolved in a mixture of chloroform: methanol (2:1) to a concentration of 1

443 mg/mL. Next, they were protonated by addition of 0.5 µL of 1 M HCl to 100 µg of PIP2,

444 kept at room temperature for 15 min and dried with nitrogen gas. The dried lipid was

445 redissolved in chloroform: methanol (3:1) mixture to 1 mg/mL followed by drying again.

446 Finally, the 100 µg of PIP2 was redissolved in 100% chloroform to 1 mg/mL and stored

447 at –20°C until used for liposome production.

448

449 **Mammalian cell culture**

450 Caco-2 (ATCC), HCT8 (ATCC) and HCT116 (ATCC) cells were cultured in RPMI-1640

451 medium (Sigma-Aldrich) supplemented with 10% fetal bovine serum (FBS), 1%

452 penicillin/streptomycin, and non-essential amino acids. Cells were cultured at 37 °C,

453 5% CO_2 and 90% humidity in 96-well plates overnight (for MTS cell viability assays),

454 Coverslip bottom 8-well chamber slide (for confocal and spinning disc confocal

455 microscopy) for 75-mm flasks (for lysosomes isolation), 24-well plates (for flow

456 cytometry) and six-well plates (for Western blot analysis).

457

458 **Antibodies**

459 Anti-MakA antiserum produced by GeneCust (1:20,000 dilution), anti-LAMP1 antibody

460 (#9091) purchased from Cell Signaling (1:1000 dilution), and anti-beta-actin antibody

461 (A2228) purchased from Sigma-Aldrich (1:5000 dilution) were used in this study.

462

463 **Cloning and purification of MakA**

464 Cloning, overexpression, and purification of MakA have been previously reported[11].

465 AlexaFluor568 labeling of MakA was performed using an AlexaFluor568 protein

466 labeling kit (Thermo Fisher) according to the manufacturer's instructions.

467

468 **Isolation and treatment of intact epithelial cell lysosomes**

14

469   HCT8 cells were grown overnight in RPMI-1640 complete media (~pH 7.2). The

470   following day cells were treated with MakA (250 nM, 18 h). At the end of treatment,

471   lysosomes were purified from vehicle or MakA-treated HCT8 cells using Lysosome

472   Isolation Kit (ab234047, Abcam), according to the manufacturer's instructions.

473

474   For the lysosome pull-down assay, intact lysosomes freshly isolated from HCT8 cells

475   were diluted in three times their volume of freshly prepared binding buffer (120 mM

476   sodium citrate, pH 5.0, pH 6.5 or pH 7.0), followed by incubation with MakA (20 μg/mL)

477   at 37°C (60 min). These MakA-lysosome complexes were centrifuged at 21,000 x g

478   (30 min, RT), pellets were washed in the respective binding buffer and resuspended in

479   2X Laemmli buffer. Samples were run on an SDS-PAGE, and after electrophoresis,

480   the samples were transferred to a nitrocellulose membrane. A Western blot analysis

481   was performed using anti-MakA antiserum (1:20,000 dilution, overnight at 4°C) that

482   was detected with HRP-conjugated goat anti-rabbit secondary antibodies. Detection of

483   LAMP1, using anti-LAMP1 antibodies, was used as an internal loading control for

484   lysosome pull-down experiments. The membranes were developed with a

485   chemiluminescence reagent (Bio-Rad). Images were acquired using an ImageQuant™

486   LAS 4000 instrument and processed using ImageJ-FIJI distribution[45].

487

488   For confocal microscopy, intact lysosomes diluted in three times their volume of freshly

489   prepared binding buffer (120 mM sodium citrate, pH 5.0, pH 6.5 or pH 7.0) were

490   exposed to Alexa568-MakA (1 μM). To facilitate the binding, Alexa568-MakA and

491   lysosomes were incubated in a 37°C incubator for 60 min. At the end of treatment,

492   samples were visualized by a Leica SP8 inverted confocal system (Leica

493   Microsystems) equipped with an HC PL APO 63x/1.40 oil immersion lens. Images were

494   captured using LasX software (Leica Microsystems) and processed using ImageJ-FIJI

495   distribution[45].

496

497   **Live cell spinning disk microscopy**

498   Live cell experiments were conducted in phenol-red-free IMDM media adjusted to pH

499   5.0 supplemented with 10% FBS and 1 mM sodium pyruvate (Thermo Fisher Scientific)

500   at 37°C in 5% CO_2. Alexa568-MakA (500 nM) was added to HCT8 cells, and images

501   were recorded every 1 min during a period of 120 min using a 63X lens and Zeiss

502   Spinning Disk Confocal controlled by ZEN interface (RRID:SCR_013672) with an Axio

15

503 Observer Z1 inverted microscope, equipped with a CSU-X1A 5000 Spinning Disk Unit

504 and an EMCCD camera iXon Ultra from ANDOR. Images were processed with Zeiss

505 ZEN Lite and ImageJ-FIJI distribution[45].

506

507 **Immunofluorescence**

508 Lysosomal tubulation was investigated by treating Caco-2 cells with Alexa568-MakA

509 (250 nM, 18 h) in IMDM complete media (pH 7.2). After treatment, cells were

510 subsequently counterstained for lysotracker (200 nM, 30 min) and Hoechst 33342 (2

511 μM, 30 min).

512

513 For confocal microscopy, HCT8 cells were loaded with the nuclear staining marker

514 Hoechst 33342 (2 μM, 30 min) and exposed to Alexa568-MakA (500 nM) in different

515 pH-adjusted IMDM complete media for 4 h at 37°C in 5% CO_2. Cells were visualized

516 live using a Leica SP8 inverted confocal system (Leica Microsystems) equipped with

517 an HC PL APO 63x/1.40 oil immersion lens. Images were captured using the LasX

518 (Leica Microsystems) and processed using ImageJ – FIJI distribution[45].

519

520 For the propidium iodide uptake experiment, HCT8 cells were treated with MakA (500

521 nM, 4 h) in IMDM complete media (pH 5.0 or pH 7.4), followed by adding propidium

522 iodide (0.5 μg/mL, 30 min). Fluorescence and bright-field images were captured with

523 a fluorescence microscope (Nikon, Eclipse Ti). Images were processed using the NIS-

524 Elements (Nikon) and ImageJ – FIJI distribution[45].

525

526 For Alexa568-MakA binding to erythrocytes, freshly prepared human erythrocytes

527 (0.25% in PBS) were loaded into an 8-well chamber slide (μ-Slide, ibidi), cells were

528 allowed to adhere to the glass surface for 10 h, followed by buffer exchange to citrate

529 buffer (pH 5.0, pH 6.5 or pH 7.4). The erythrocytes were exposed to Alexa568-MakA

530 (500 nM) for 3 h at 37°C in 5% CO_2. Cells were visualized using a Leica SP8 inverted

531 confocal system (Leica Microsystems) equipped with an HC PL APO 63x/1.40 oil

532 immersion lens. The maximum z-stack projection of the human erythrocytes treated

533 with Alexa568-MakA (pH 6.5 in citrate buffer) was constructed using Leica LasX

534 Software.

535

536 **Cell toxicity assay**

16

537 HCT8, Caco-2 and HCT116 cells were treated with increasing concentrations of MakA

538 at a given pH at the indicated time point (4 h or 24 h). At the end of treatment, cells

539 were incubated with MTS reagent (15 min) at 37°C in an incubator, and cell viability

540 was quantified by measuring MTS absorbance on an Infinite M200 microplate reader

541 (Tecan). Data were normalized to the vehicle-treated cells (pH 7.2) and expressed as

542 a percentage of the control.

543

544 For flow cytometry experiments, HCT8 cells were grown on a 24-well plate ($8x10^4$/well,

545 Tecan Group Ltd) overnight in IMDM complete media (pH 7.2). The following day, cells

546 were treated with vehicle (Tris 20 mM) or MakA (500 nM, 4 h) in media adjusted to a

547 given pH. At the end of treatment, cells were incubated with propidium iodide (0.5

548 µg/mL) at 37°C for 30 min. Cellular uptake of propidium iodide in vehicle or MakA-

549 treated cells was investigated by flow cytometry. Cellular uptake of propidium iodide

550 was quantified and presented as mean fluorescence intensity (MFI) for the gated cells.

551

552 **Human erythrocytes hemolysis assay**

553 Freshly prepared human erythrocytes (0.25%) in citrate buffer (120 mM sodium citrate,

554 pH adjusted to 5.0, 6.5 or 7.4) were added to a 96-well plate. The erythrocytes were

555 treated with increasing concentrations of MakA at two different time points (90 min and

556 5 h) at 37°C in 5% CO_2. After centrifugation (500 x g), the supernatants were monitored

557 spectrophotometrically for released hemoglobin by measuring absorbance at 545 nm

558 to indicate red blood cell lysis. MakA-induced hemolysis of erythrocytes was

559 normalized against erythrocytes treated with Triton X-100 (0.1%). Data were

560 expressed as a percentage.

561

562 **Scanning Electron Microscopy**

563 Freshly prepared human erythrocytes (0.25%) were treated with MakA (500 nM, 90

564 min) in citrate buffer (120 mM, pH 6.5). Samples were fixed with a fixative (1%

565 glutaraldehyde + 0.1 M CaCo buffer + 3 mM $MgCl_2$) in the microwave and washed

566 twice with buffer (0.1 M CaCo buffer + 2.5% sucrose + 3 mM $MgCl_2$). They were

567 sedimented onto poly-L-lysine-coated coverslips for 1 h and subsequently dehydrated

568 in series of graded ethanol solutions in the microwave. The samples were then dried

569 to a critical point (Leica EM300). Subsequently, samples were coated with 2 nm of

570 platinum (Quorum Q150T ES). Samples were imaged with field-emission scanning

17

571 electron microscopy (FESEM; Carl Zeiss Merlin) using an in-chamber (ETD)

572 secondary electron detector at an accelerating voltage of 5 kV and probe current of

573 150 pA.

574

575 **Extraction of epithelial cell lipids for liposome binding assays**

576 Lipids were extracted by the Folch method[46] from 10 x 150 cm^2 confluent flasks of

577 HCT8 cells. Briefly, the HCT8 cell lipid extracts, dissolved in chloroform, were dried to

578 a thin film under a nitrogen stream. The dried lipid yield was 12 mg. The lipid film (5 or

579 10 mg/mL) was hydrated in HEPES buffer (10 mM HEPES, 150 mM NaCl, pH 7.4),

580 citrate buffer (120 mM citrate buffer, pH 6.5) or (20 mM citric acid, 50 mM KCl, 0.1 mM

581 EDTA, pH 4.5). The lipid suspension was extruded through polycarbonate membranes

582 (0.1 µm) using the Avanti Mini-Extruder (Avanti Polar Lipids, Alabaster, AL, USA).

583

584 The liposome pull-down assay was performed as previously described[21,47]. Briefly, the

585 liposome suspension was diluted in five times its volume of freshly prepared binding

586 buffer (120 mM sodium citrate, pH 5.0, pH 6.5 or pH 7.4), followed by centrifugation at

587 21,000 x g for 30 min at room temperature. The liposome pellet was resuspended in

588 binding buffer followed by incubation with MakA (20 µg/mL). The liposome-protein

589 mixtures were incubated at 37°C (60 min), followed by centrifugation at 21,000 x g at

590 room temperature (30 min). To reduce the background, pellets were washed in the

591 respective binding buffer two to three times. The resulting sample was loaded onto the

592 SDS-PAGE, transferred to a nitrocellulose membrane and subjected to Western blot

593 analysis using anti-MakA antiserum (1:10,000 dilution, overnight at 4°C). The MakA

594 antibodies were detected with HRP-conjugated goat anti-rabbit secondary antibodies.

595 The membranes were developed with a chemiluminescence reagent (Bio-Rad).

596 Images were acquired using ImageQuant LAS 4000 instrument and processed using

597 ImageJ - FIJI distribution[45].

598

599 **Circular dichroism spectroscopy**

600 Far-UV Circular Dichroism (CD) analysis of MakA protein or MakA and ECLE liposome

601 complexes was performed using Jasco J-720 Spectropolarimeter (Japan) at 25°C.

602 Briefly, MakA (3 µM) alone or MakA (3 µM) and ECLE (5 mg/mL) were incubated

603 overnight at 25°C in citrate buffer (5 mM) with varying pH. The spectra were recorded

604 between 195-260 nm using 2-s response time, a 1 mm cuvette path length and a 2 nm

18

605 bandwidth. Data of an average of five repeated scans were used for graphical
606 presentation and analyses.

607

608 **Liposome preparation**

609 Liposomes containing 0.5 mol% PEG5Kce, 5 mol% PIP2, 10 mol% SM, 10 mol%
610 POPS, 15 mol% DOPE, 20 mol% Chol, and 39.5 mol% POPC (referred to herein as
611 synthetic lipid mixture [SLM] liposomes) were prepared using the lipid film hydration
612 and extrusion method. SLM+TxRed liposomes were created using the same protocol
613 as above except for the addition of 1 mol% TxRed-DHPE and the corresponding
614 reduction of POPC content to 38.5 mol%. The individual lipids dissolved in chloroform
615 were mixed together, dried under nitrogen and then stored in a vacuum for a minimum
616 of one hour. The dried lipid film was then rehydrated using a pre-heated citrate-
617 potassium buffer at pH 4.5 (20 mM citric acid, 50 mM KCl, pH 4.5, 40°C) to a lipid
618 concentration of 1 mg/mL. The solution was then extruded at ~40°C eleven times
619 through a polycarbonate membrane with 100-nm pore size using an Avanti mini
620 extruder. The liposomes were stored at 4°C until used.

621

622 **Fluorescence microscopy of SLBs**

623 Supported lipid bilayers (SLBs) were formed on glass coverslips. Coverslips were
624 cleaned by boiling in 7X detergent (MP biochemicals) for 2 h followed by extensive
625 rinsing in 18 MΩ water and blown dried with nitrogen. Clean coverslips were fitted with
626 Poly(dimethylsiloxane) (PDMS) sheets containing 10 μm holes to create glass-
627 bottomed wells. SLBs were made by adding 10 μL of 0.1 mg/mL of either SLM or
628 SLM+TxRed liposomes to each well and incubating the wells at 37°C for 30 min before
629 rinsing the wells with citrate-potassium buffer to remove excess liposomes. Wells were
630 then extensively rinsed with citrate buffer at pH 6.5 (120 mM sodium citrate) prior to
631 protein addition. Either Alexa568-MakA or unlabeled MakA diluted in citrate buffer at
632 pH 6.5 was then added to a well to reach a final concentration of 3 μM. The SLB surface
633 was monitored using a Nikon Eclipse Ti2-E inverted epifluorescence microscope
634 equipped with a 60X objective multi-band pass filter cube 86012v2
635 DAPI/FITC/TxRed/Cy5 (Nikon Corp.), Prime 95B sCMOS camera (Teledyne
636 Photometrics), and Spectra III light source (Lumencor).

637

638 **Surface plasmon resonance**

19

639   To analyze the interaction of MakA with ECLE or POPC liposomes, L1 sensor chips

640   and a Biacore 3000 instrument were used as previously described[21]. In brief, the ECLE

641   or POPC liposomes were immobilized onto the cells of the L1 sensor chip surfaces at

642   low flow rates of 2 µL/min for 40 min, stabilized with 50 mM NaOH, and the successful

643   surface coverage was tested by injecting Bovine Serum Albumin (BSA). After

644   successful surface coverage, two-fold serially diluted MakA (diluted in the SPR running

645   buffer (120 mM citrate buffer, pH 6.5) with increasing concentrations (0 to 200 nM) was

646   injected for 120 sec at flow rates of 5 µL/min. For the binding analysis with POPC

647   liposomes, the maximum concentration of MakA (200 nM) was used. All experiments

648   were repeated at least twice, and the backgrounds of control flow cells were subtracted

649   from the experimental cells before final data processing. The binding affinities (KD)

650   were determined from the concentration gradient experiments, and the binding

651   responses at equilibrium were fit to a simple 1:1 steady-state affinity model using the

652   global data analysis option available within the Scrubber 2 software

653   (http://www.biologic.com.au/scrubber.html).

654

655   **Western blot analysis**

656   For Western blot analysis, HCT8 cells were grown on a 6-well slide (3×10^5/well,

657   Thermo Scientific) overnight. The pH of IMDM cell culture media supplemented with

658   10% FBS and 1% penicillin/streptomycin was adjusted to either 5.0, 6.5, 7.4 or 8.0

659   followed by treatment with an increasing concentration of MakA for 4 h. Cells were

660   rinsed with ice-cold PBS to remove unbound MakA and lysed in ice-cold NP-40 cell

661   lysis buffer (20 mM Tris-HCl pH 8, 0.25% Nonidet P-40, 10% glycerol, 0.5 mM EDTA,

662   300 mM KCl, 0.5 mM EGTA, 1x phosSTOP, and protease inhibitor cocktail from

663   Roche). After mixing with sample buffer, cell lysates were boiled for 5 min and

664   separated by SDS-PAGE. The proteins were transferred to a nitrocellulose membrane

665   and blocked with 5% skim milk in 0.1% PBST (RT, 1 h). The membranes were

666   incubated with respective primary antibodies in 5% skim milk (4°C, overnight). After

667   washing with PBST (0.1%), membranes were incubated with HRP-conjugated

668   secondary antibodies in 5% skim milk (RT, 1 h). The membranes were developed with

669   Immun-Star™ AP Chemiluminescence (Bio-Rad). Images were acquired using

670   ImageQuant LAS 4000 instrument and processed using ImageJ - FIJI distribution[45].

671

672   **Transmission electron microscopy**

20

673 Negative staining for lysosomes or liposomes was performed on glow discharged

674 copper grids (300 mesh) coated with a thin carbon film (Ted Pella, Redding, CA). After

675 adding 3 μL sample to the grids, they were washed twice with MQ water and stained

676 with 1.5% uranyl acetate solution (EMS [Hatfield, PA]), followed by MQ water washing.

677 Grids were examined with Talos L120C, operating at 120 kV. Transmission electron

678 micrographs (TEM) were acquired with a Ceta 16M CCD camera using TEM Image &

679 Analysis software ver. 4.17 (FEI, Eindhoven, The Netherlands).

680

Cryo-electron microscopy sample preparation and data collection

682 The ECLE liposomes (10 mg/mL) were incubated with MakA (30 μM) in binding buffer

683 (120 mM sodium citrate, pH 6.5) for 60 min at 37°C. Quantifoil 2/1-200 grids were glow

684 discharged before the addition of 3 μL protein-liposome mixture. Grids were then flash-

685 frozen in liquid ethane using an FEI Vitrobot (Thermo Fisher Scientific). Data collection

686 was performed at the Umeå University Core Facility for Electron Microscopy (UCEM)

687 on a Titan Krios (Thermo Fisher Scientific), operating at 300 kV and equipped with a

688 Gatan K2 BioQuantum direct electron detector (Gatan, Inc.). Images were acquired

689 using EPU (Thermo Fisher Scientific). A total of 2,476 movies, each with 40 frames

690 over a total dose of 43 e-/Å^2, and a 0.75 to 2.5 μm defocus range at a 1.042 Å pixel

691 size were collected.

692

Cryo-EM data processing and helical reconstruction

694 The MotionCorr implementation of RELION-3.1 was used for drift correction and dose

695 weighting of the micrographs[48]. The contrast transfer function (CTF) was determined

696 using CTFFIND-4.1.14 (ref.[49]), and empty or micrographs with poor CTF fits or low ice

697 quality were removed after manual inspection, which reduced the total to 1,351

698 micrographs (**Supplementary Fig. 4**). Helical reconstruction tools in RELION-3.1 (ref.

699 [50]) were used for subsequent image processing. Filaments were selected manually

700 using the helix picker in RELION-3.1 with an outcome of 13,784 picked start and

701 endpoints. First, segments were extracted between the picked start and endpoints as

702 2x binned data using a box size of 437 Å (210 pixels, 2.084 Å/px) with an inter-box

703 distance (IBD) of 23 Å, resulting in 195'809 segments, which were subjected to 2D

704 classification with 80 classes and a spherical mask of 360 Å. Classes displaying a

705 straight filament with high-resolution features (152'961 segments) were refined without

706 symmetry using a featureless cylinder (diameter 320 Å) generated with the helix

21

707 toolbox in RELION-3.1 (**Supplementary Fig. 4**). In parallel, a 2D classification was

708 performed by extracting 65'241 segments from 2x binned data, applying a box size of

709 646 Å (310 px, 2.084 Å/px), an IBD of 62 Å, and a spherical mask of 580 Å. The volume

710 refined without symmetry and the 2D class averages obtained from large helical

711 segments were used to determine the helical symmetry parameters. Diameter and

712 repeat distance were visually analyzed and measured in a representative 2D class

713 average in RELION-3.1 (**Fig. 4b and Supplementary Fig. 5a**). Additionally, the repeat

714 distance was calculated from the corresponding collapsed power spectrum (layer-line

715 distance-1) in SPRING-0.68 (ref. [51]) (**Supplementary Fig. 5b**). Next, to determine the

716 helical twist and rise, the number of turns and subunits per repeat were counted from

717 the initial reconstructed model (**Supplementary Fig. 5c-d**), and the handedness of the

718 reconstruction was, after the subsequent high-resolution refinement described below,

719 confirmed using the MakA crystal structure[11].

720

721 For the final reconstruction, 95'603 segments were extracted unbinned with 460-pixel

722 boxes (479 Å) and an IBD of 46.56 Å. Subsequent 2D classification with a 432 Å

723 spherical mask resulted in 65'485 segments that were 3D refined using a featureless

724 cylinder as a template and a spherical mask of 360 Å. Local symmetry searches were

725 performed to narrow down the helical symmetry by refining helical twist (48-50˚) and

726 rise (5.4-6 Å), yielding a map with an overall 4.1 Å resolution. Subsequent Bayesian

727 polishing improved the resolution to 3.8 Å, and estimation of anisotropic magnification

728 and CTF refinement resulted in a final map with an overall resolution of 3.7 Å

729 (**Supplementary Fig. 6**). As the peripheral region was less well-resolved, a subsection

730 of the structure was isolated via signal subtraction, centered in a 260-pixel box and

731 subjected to 3D classification without symmetry and local searches with increasing

732 sampling rate from 3.7˚, 1.8˚, and 0.9˚ angles. From the resulting three classes, further

733 refinement of class 2 (56.8%) yielded a map of the two tetramers in isolation at an

734 overall resolution of 4.1 Å with improved peripheral density (**Supplementary Fig. 4**,

735 blue branch, **and Supplementary Fig. 6d,e**). As the resulting three classes showed

736 different conformations of the MakA head region, we examined whether these

737 conformations exist across the volume. Two subsequent 3D classifications into five

738 classes, without image alignment but with local symmetry searches, first with all

739 classes, then with the top class from the first run, showed a normal distribution of

740 angles, ranging from 48.48˚ to 48.68˚ suggesting continuous motion/rotation along the

22

741　filament axis, which is most pronounced in the tail region (**Supplementary Fig. 4,** blue

742　branch, lower right).

743

744　**Model building, refinement, and validation**

745　To obtain an initial model of the tail domain, the MakA crystal structure (PDB-6EZV[11])

746　was rigid-body docked into the density map using Chimera[52] and Coot[53]. Regions

747　where the density/model fit was poor (no density, difference in conformation) were

748　trimmed. This included the C-terminal tail (res. 351-365) and the central region (res.

749　~160-260). Elements in the tail domain with poor density fit were rigid-body docked.

750　The central region of the protein, which includes the neck and head, was built *de novo*

751　in Coot[53]. The model was first refined against the asymmetric map of the two tetramers

752　in isolation (4.1 Å) using phenix.real_space_refine (version 1.14-3260)[54]. Next, this

753　model was rigid-body docked into the 3.7-Å helical map, two neighboring placeholder

754　molecules were symmetry expanded to provide interaction interfaces, and refined with

755　secondary structure restraints. The final model contains four MakA subunits with

756　trimmed sidechains in the tail domain (N-terminus to 159, 281 to C-terminus,

757　**Supplementary Fig. 6e,f**). To validate the final model, all atomic coordinates were

758　displaced randomly by 0.5 Å, refined against half map 1, followed by calculating the

759　Fourier-Shell Correlation coefficient of the resulting refined model, and half map 1 or

760　half map 2 (ref [55]). Model statistics are presented in (**Supplementary Table S1**).

761

762　**Map and model visualization**

763　Structure analyses and preparation of the figures were performed using PyMOL

764　(Schrödinger) or UCSF ChimeraX[56].

765

766　**Statistical analysis**

767　The result from replicates is presented as mean ± s.e.m. or mean ± s.d. The statistical

768　significance of different groups was determined by Student's t-tests (two-tailed,

769　unpaired) or one-way ANOVA using Microsoft Excel or GraphPad Prism. *$p \leq 0.05$, **p

770　≤ 0.01, ns = not significant.

771
772

DATA AVAILABILITY

The cryo-EM density maps have been deposited in the EM Data Bank with accession code EMD-13185 (MakA helical reconstruction) and EMD-13185-additional map 1 (two tetramers refined in isolation). Coordinates have been deposited in the Protein Data Bank under accession code PDB-7P3R.

References

1   Geny, B. & Popoff, M. R. Bacterial protein toxins and lipids: pore formation or toxin entry into cells. *Biol Cell* **98**, 667-678, doi:10.1042/BC20050082 (2006).

2   Lemichez, E. & Barbieri, J. T. General aspects and recent advances on bacterial protein toxins. *Cold Spring Harb Perspect Med* **3**, a013573, doi:10.1101/cshperspect.a013573 (2013).

3   Los, F. C., Randis, T. M., Aroian, R. V. & Ratner, A. J. Role of pore-forming toxins in bacterial infectious diseases. *Microbiol Mol Biol Rev* **77**, 173-207, doi:10.1128/MMBR.00052-12 (2013).

4   Verma, P., Gandhi, S., Lata, K. & Chattopadhyay, K. Pore-forming toxins in infection and immunity. *Biochem Soc Trans*, doi:10.1042/BST20200836 (2021).

5   Bischofberger, M., Iacovache, I. & van der Goot, F. G. Pathogenic pore-forming proteins: function and host response. *Cell Host Microbe* **12**, 266-275, doi:10.1016/j.chom.2012.08.005 (2012).

6   Clemens, J. D., Nair, G. B., Ahmed, T., Qadri, F. & Holmgren, J. Cholera. *Lancet* **390**, 1539-1549, doi:10.1016/S0140-6736(17)30559-7 (2017).

7   Kaper, J. B., Fasano, A. & Trucksis, M. *Toxins of Vibrio cholerae. In: Vibrio cholerae and cholera: Molecular to global perspectives*. (American Society for Microbiology Press, Washington, DC., 1994).

8   Taylor, R. K., Miller, V. L., Furlong, D. B. & Mekalanos, J. J. Use of phoA gene fusions to identify a pilus colonization factor coordinately regulated with cholera toxin. *Proc Natl Acad Sci U S A* **84**, 2833-2837, doi:10.1073/pnas.84.9.2833 (1987).

9   Rajpara, N. *et al.* Synergistic effect of various virulence factors leading to high toxicity of environmental V. cholerae non-O1/ non-O139 isolates lacking ctx gene : comparative study with clinical strains. *PLoS One* **8**, e76200, doi:10.1371/journal.pone.0076200 (2013).

10   Schwartz, K., Hammerl, J. A., Gollner, C. & Strauch, E. Environmental and Clinical Strains of Vibrio cholerae Non-O1, Non-O139 From Germany Possess Similar Virulence Gene Profiles. *Front Microbiol* **10**, 733, doi:10.3389/fmicb.2019.00733 (2019).

11   Dongre, M. *et al.* Flagella-mediated secretion of a novel Vibrio cholerae cytotoxin affecting both vertebrate and invertebrate hosts. *Commun Biol* **1**, 59, doi:10.1038/s42003-018-0065-z (2018).

12   Tsou, A. M. & Zhu, J. Quorum sensing negatively regulates hemolysin transcriptionally and posttranslationally in Vibrio cholerae. *Infect Immun* **78**, 461-467, doi:10.1128/IAI.00590-09 (2010).

13   Nadeem, A. *et al.* A tripartite cytolytic toxin formed by Vibrio cholerae proteins with flagellum-facilitated secretion. *bioRxiv*, 2021.2006.2020.449157, doi:10.1101/2021.06.20.449157 (2021).

24

820   14   Oscarsson, J., Mizunoe, Y., Uhlin, B. E. & Haydon, D. J. Induction of haemolytic
821   activity in Escherichia coli by the slyA gene product. *Mol Microbiol* **20**, 191-199,
822   doi:10.1111/j.1365-2958.1996.tb02500.x (1996).
823   15   Oscarsson, J. *et al.* Molecular analysis of the cytolytic protein ClyA (SheA) from
824   Escherichia coli. *Mol Microbiol* **32**, 1226-1238, doi:10.1046/j.1365-
825   2958.1999.01435.x (1999).
826   16   Brauning, B. *et al.* Structure and mechanism of the two-component alpha-helical pore-
827   forming toxin YaxAB. *Nat Commun* **9**, 1806, doi:10.1038/s41467-018-04139-2
828   (2018).
829   17   Schubert, E., Vetter, I. R., Prumbaum, D., Penczek, P. A. & Raunser, S. Membrane
830   insertion of alpha-xenorhabdolysin in near-atomic detail. *Elife* **7**,
831   doi:10.7554/eLife.38017 (2018).
832   18   Sastalla, I. *et al.* The Bacillus cereus Hbl and Nhe tripartite enterotoxin components
833   assemble sequentially on the surface of target cells and are not interchangeable. *PLoS*
834   *One* **8**, e76955, doi:10.1371/journal.pone.0076955 (2013).
835   19   Wilson, J. S. *et al.* Identification and structural analysis of the tripartite α-pore forming
836   toxin of Aeromonas hydrophila. *Nature Communications* **10**, 2900,
837   doi:10.1038/s41467-019-10777-x (2019).
838   20   Churchill-Angus, A. M. *et al.* Characterisation of a tripartite alpha-pore forming toxin
839   from Serratia marcescens. *Sci Rep* **11**, 6447, doi:10.1038/s41598-021-85726-0 (2021).
840   21   Nadeem, A. *et al.* Phosphatidic acid-mediated binding and mammalian cell
841   internalization of the Vibrio cholerae cytotoxin MakA. *PLoS Pathog* **17**, e1009414,
842   doi:10.1371/journal.ppat.1009414 (2021).
843   22   Nadeem, A. *et al.* Suppression of beta-catenin signaling in colon carcinoma cells by a
844   bacterial protein. *Int J Cancer*, doi:10.1002/ijc.33562 (2021).
845   23   Corkery, D. P. *et al.* Vibrio cholerae cytotoxin MakA induces noncanonical autophagy
846   resulting in the spatial inhibition of canonical autophagy. *J Cell Sci*,
847   doi:10.1242/jcs.252015 (2020).
848   24   Beecher, D. J. & Wong, A. C. Tripartite hemolysin BL from Bacillus cereus.
849   Hemolytic analysis of component interactions and a model for its characteristic
850   paradoxical zone phenomenon. *J Biol Chem* **272**, 233-239 (1997).
851   25   Wilson, J. S. *et al.* (Identification and structural analysis of the tripartite alpha-pore
852   forming toxin of Aeromonas hydrophila). *Nat Commun* **10**, 2900, doi:10.1038/s41467-
853   019-10777-x (2019).
854   26   Lorizate, M. *et al.* Comparative lipidomics analysis of HIV-1 particles and their
855   producer cell membrane in different cell lines. *Cell Microbiol* **15**, 292-304,
856   doi:10.1111/cmi.12101 (2013).
857   27   Ganash, M. *et al.* Structure of the NheA component of the Nhe toxin from Bacillus
858   cereus: implications for function. *PLoS One* **8**, e74748,
859   doi:10.1371/journal.pone.0074748 (2013).
860   28   Kovac, J. *et al.* Production of hemolysin BL by Bacillus cereus group isolates of dairy
861   origin is associated with whole-genome phylogenetic clade. *BMC Genomics* **17**, 581,
862   doi:10.1186/s12864-016-2883-z (2016).
863   29   Madegowda, M., Eswaramoorthy, S., Burley, S. K. & Swaminathan, S. X-ray crystal
864   structure of the B component of Hemolysin BL from Bacillus cereus. *Proteins* **71**,
865   534-540, doi:10.1002/prot.21888 (2008).
866   30   Wallace, A. J. *et al.* E. coli hemolysin E (HlyE, ClyA, SheA): X-ray crystal structure
867   of the toxin and observation of membrane pores by electron microscopy. *Cell* **100**,
868   265-276, doi:10.1016/s0092-8674(00)81564-0 (2000).

869 31   Ghosal, D. & Lowe, J. Collaborative protein filaments. *EMBO J* **34**, 2312-2320,
870   doi:10.15252/embj.201591756 (2015).
871 32   Pezeshkian, W. *et al.* Membrane invagination induced by Shiga toxin B-subunit: from
872   molecular structure to tube formation. *Soft Matter* **12**, 5164-5171,
873   doi:10.1039/c6sm00464d (2016).
874 33   Koehler, T. M. & Collier, R. J. Anthrax toxin protective antigen: low-pH-induced
875   hydrophobicity and channel formation in liposomes. *Mol Microbiol* **5**, 1501-1506,
876   doi:10.1111/j.1365-2958.1991.tb00796.x (1991).
877 34   Ni, T. *et al.* Structure and mechanism of bactericidal mammalian perforin-2, an
878   ancient agent of innate immunity. *Sci Adv* **6**, eaax8286, doi:10.1126/sciadv.aax8286
879   (2020).
880 35   Sathyanarayana, P. *et al.* Cholesterol promotes Cytolysin A activity by stabilizing the
881   intermediates during pore formation. *Proc Natl Acad Sci U S A* **115**, E7323-E7330,
882   doi:10.1073/pnas.1721228115 (2018).
883 36   Gellings, P. S. & McGee, D. J. Arcanobacterium haemolyticum Phospholipase D
884   Enzymatic Activity Promotes the Hemolytic Activity of the Cholesterol-Dependent
885   Cytolysin Arcanolysin. *Toxins (Basel)* **10**, doi:10.3390/toxins10060213 (2018).
886 37   Rosado, C. J. *et al.* The MACPF/CDC family of pore-forming toxins. *Cell Microbiol*
887   **10**, 1765-1774, doi:10.1111/j.1462-5822.2008.01191.x (2008).
888 38   Fiertel, A. & Klein, H. P. On sterols in bacteria. *J Bacteriol* **78**, 738-739,
889   doi:10.1128/jb.78.5.738-739.1959 (1959).
890 39   Watts, J. L. & Ristow, M. Lipid and Carbohydrate Metabolism in Caenorhabditis
891   elegans. *Genetics* **207**, 413-446, doi:10.1534/genetics.117.300106 (2017).
892 40   Chinnapen, D. J. *et al.* Lipid sorting by ceramide structure from plasma membrane to
893   ER for the cholera toxin receptor ganglioside GM1. *Dev Cell* **23**, 573-586,
894   doi:10.1016/j.devcel.2012.08.002 (2012).
895 41   Romer, W. *et al.* Shiga toxin induces tubular membrane invaginations for its uptake
896   into cells. *Nature* **450**, 670-675, doi:10.1038/nature05996 (2007).
897 42   Safouane, M. *et al.* Lipid cosorting mediated by shiga toxin induced tubulation. *Traffic*
898   **11**, 1519-1529, doi:10.1111/j.1600-0854.2010.01116.x (2010).
899 43   Campelo, F. Modeling morphological instabilities in lipid membranes with anchored
900   amphiphilic polymers. *Journal of Chemical Biology* **2**, 65–80, doi:DOI
901   10.1007/s12154-009-0020-z (2007).
902 44   Nadeem, A. *et al.* Protein receptor-independent plasma membrane remodeling by
903   HAMLET: a tumoricidal protein-lipid complex. *Sci Rep* **5**, 16432,
904   doi:10.1038/srep16432 (2015).
905 45   Schindelin, J. *et al.* Fiji: an open-source platform for biological-image analysis. *Nat
906   Methods* **9**, 676-682, doi:10.1038/nmeth.2019 (2012).
907 46   Folch, J., Lees, M. & Sloane Stanley, G. H. A simple method for the isolation and
908   purification of total lipides from animal tissues. *J Biol Chem* **226**, 497-509 (1957).
909 47   Julkowska, M. M., Rankenberg, J. M. & Testerink, C. Liposome-binding assays to
910   assess specificity and affinity of phospholipid-protein interactions. *Methods Mol Biol*
911   **1009**, 261-271, doi:10.1007/978-1-62703-401-2_24 (2013).
912 48   Zivanov, J. *et al.* New tools for automated high-resolution cryo-EM structure
913   determination in RELION-3. *Elife* **7**, doi:10.7554/eLife.42166 (2018).
914 49   Rohou, A. & Grigorieff, N. CTFFIND4: Fast and accurate defocus estimation from
915   electron micrographs. *J Struct Biol* **192**, 216-221, doi:10.1016/j.jsb.2015.08.008
916   (2015).
917 50   He, S. & Scheres, S. H. W. Helical reconstruction in RELION. *J Struct Biol* **198**, 163-
918   176, doi:10.1016/j.jsb.2017.02.003 (2017).

919 51   Desfosses, A., Ciuffa, R., Gutsche, I. & Sachse, C. SPRING - an image processing
920   package for single-particle based helical reconstruction from electron
921   cryomicrographs. *J Struct Biol* **185**, 15-26, doi:10.1016/j.jsb.2013.11.003 (2014).
922 52   Pettersen, E. F. *et al.* UCSF Chimera--a visualization system for exploratory research
923   and analysis. *J Comput Chem* **25**, 1605-1612, doi:10.1002/jcc.20084 (2004).
924 53   Emsley, P. & Cowtan, K. Coot: model-building tools for molecular graphics. *Acta
925   Crystallogr D Biol Crystallogr* **60**, 2126-2132, doi:10.1107/S0907444904019158
926   (2004).
927 54   Adams, P. D. *et al.* PHENIX: a comprehensive Python-based system for
928   macromolecular structure solution. *Acta Crystallogr D Biol Crystallogr* **66**, 213-221,
929   doi:10.1107/S0907444909052925 (2010).
930 55   Brown, A. *et al.* Tools for macromolecular model building and refinement into
931   electron cryo-microscopy reconstructions. *Acta Crystallogr D Biol Crystallogr* **71**,
932   136-153, doi:10.1107/S1399004714021683 (2015).
933 56   Goddard, T. D. *et al.* UCSF ChimeraX: Meeting modern challenges in visualization
934   and analysis. *Protein Sci* **27**, 14-25, doi:10.1002/pro.3235 (2018).
935
936

956

957 **AUTHOR CONTRIBUTIONS**

27

958   A.N. performed confocal microscopy, transmission electron microscopy, cryo-electron

959   microscopy sample preparation for data collection, flow cytometry and cell toxicity; K.P.

960   purified protein; E.T. and S.L.M, assisted A.N. with Western blot. A.N., H.P., E.T., At.

961   A. and M.B. performed liposome experiments. At. A., and J.Å., performed CD

962   experiments. A.B. and J.B. performed cryo-EM data processing and analysis. N. Z.

963   assisted A.N. with hemolytic assay and analyzed the *mak* operon. A.N. wrote the initial

964   version of the manuscript. All authors read and commented on the manuscript. M.B.,

965   K.P., A.S., G.G., B.E.U., and S.N.W. obtained the funding. A. N., M.B., K.P., B.E.U,

966   and S.N.W. supervised the research and finalized the manuscript.

967

968   **COMPETING INTERESTS STATEMENT**

969   S.N.W., B.E.U., A.N., and K.P. wish to make the disclosure that we are named

970   inventors in a PCT application (*Vibrio cholerae* protein for use against cancer)

971   published under No. WO 2021/071419. This does not alter our adherence to

972   eLife policies on sharing data and materials.

28

973
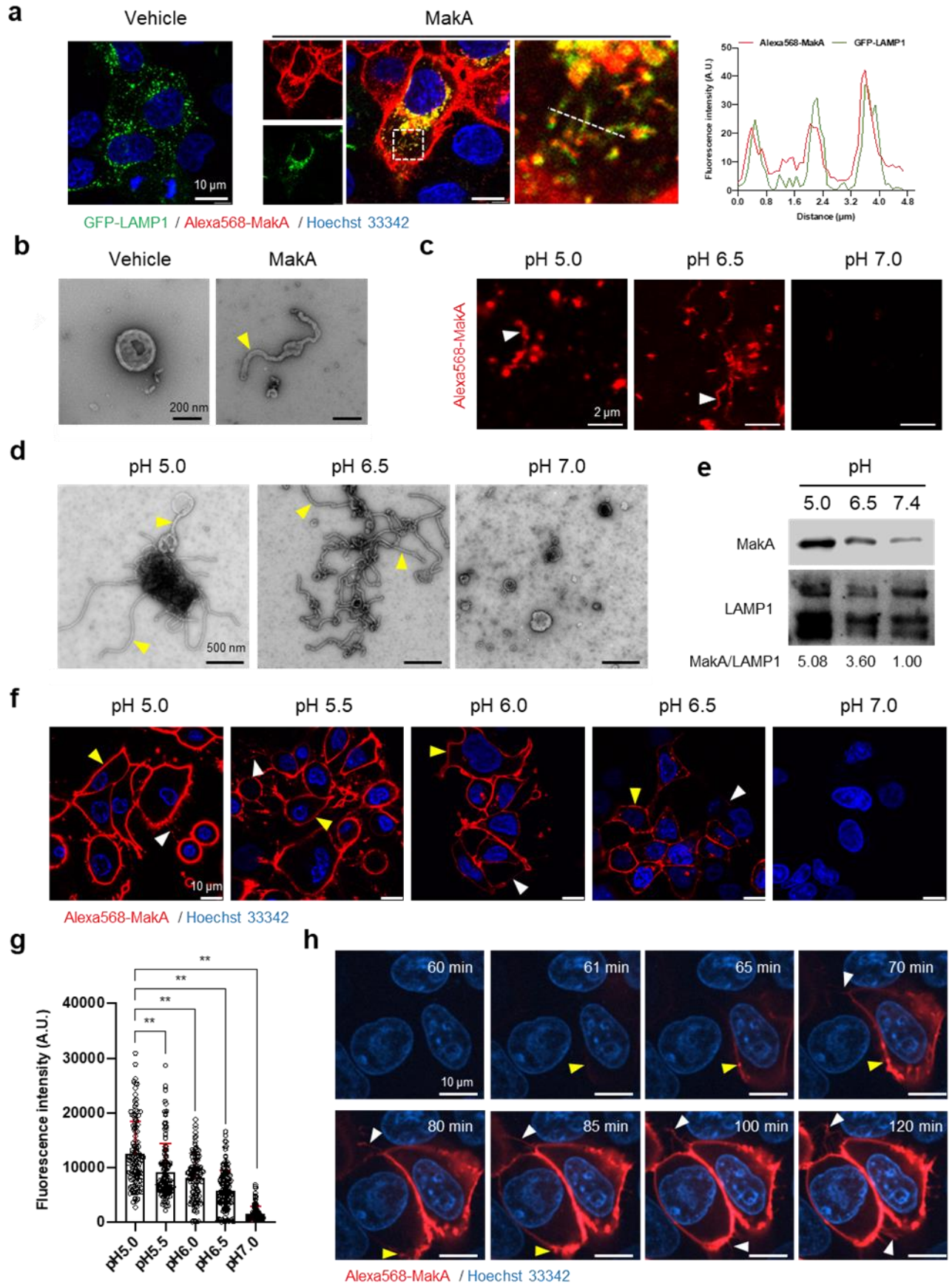
Fig. 1: pH-dependent tubulation of lysosomes and binding to epithelial cells by MakA

a Caco-2 cells transfected with GFP-LAMP1 were treated with vehicle or Alexa568-MakA (250 nM, 18 h). Nuclei were counterstained with Hoechst 33342. The line graph to the right indicates the accumulation of Alexa568-MakA in GFP-LAMP1-positive tubular lysosomes. Pearson correlation co-efficient was used to calculate Alexa568-MakA (red) co-localization with GFP-LAMP1 (green) along with the tubular structures. Scale bars, 10 μm. **b** Representative electron micrographs of lysosomes purified from vehicle and MakA (250 nM, 24 h) treated HCT8 cells. Scale bars, 200 nm. The yellow arrowhead indicates a tubular structure found with lysosomes from MakA-treated cells. **c** The pH-dependent binding of Alexa568-MakA to purified lysosomes isolated from HCT8 cells: White arrowheads point to the tubular structures observed with MakA-treated purified lysosomes. Images shown for specimens from different pH conditions were acquired using the same settings of the microscope. Scale bars, 2 μm**. d** Representative electron micrographs of purified lysosomes treated with MakA (1 μM) under different pH conditions. Yellow arrowheads indicate tubular structures appearing at low pH. Scale bars, 500 nm. **e** Western blot analysis of samples from lysosome pull-down assays performed with lysosomes treated with MakA (250 nM, 60 min) under different pH conditions. Lysosome-bound MakA was detected with anti-MakA antiserum. Immunodetection of LAMP1 was used as a reference and the MakA/LAMP1 ratio was determined for the quantification of relative MakA amounts. **f** HCT8 cells were exposed to Alexa568-MakA (500 nM, 4 h) under different pH conditions and visualized live under by confocal microscopy. Nuclei were counterstained with Hoechst 33342 (blue). Yellow arrowheads indicate cell membrane association, while white arrowheads indicate MakA-positive tubular structures. The different images were acquired using the same microscope settings. Scale bars, 10 μm. **g** The histogram indicates quantification of cell-bound Alexa568-MakA (n = 100 cells) as shown in (f). Data from two independent experiments are presented as mean ± s.e.m.; one-way analysis of variance (ANOVA) with Dunnett's multiple comparisons test. **p≤0.01. **h** Still images of HCT8 cells exposed to Alexa568-MakA (500 nM) at pH 5.0. Yellow arrowheads indicate the initial binding site of MakA and white arrowheads indicate the appearance of MakA-positive tubular structures in a time-dependent manner. Nuclei were counterstained with Hoechst 33342. Scale bars, 10 μm.

Source data for figure 1e; Uncropped MakA-detected membrane.

30
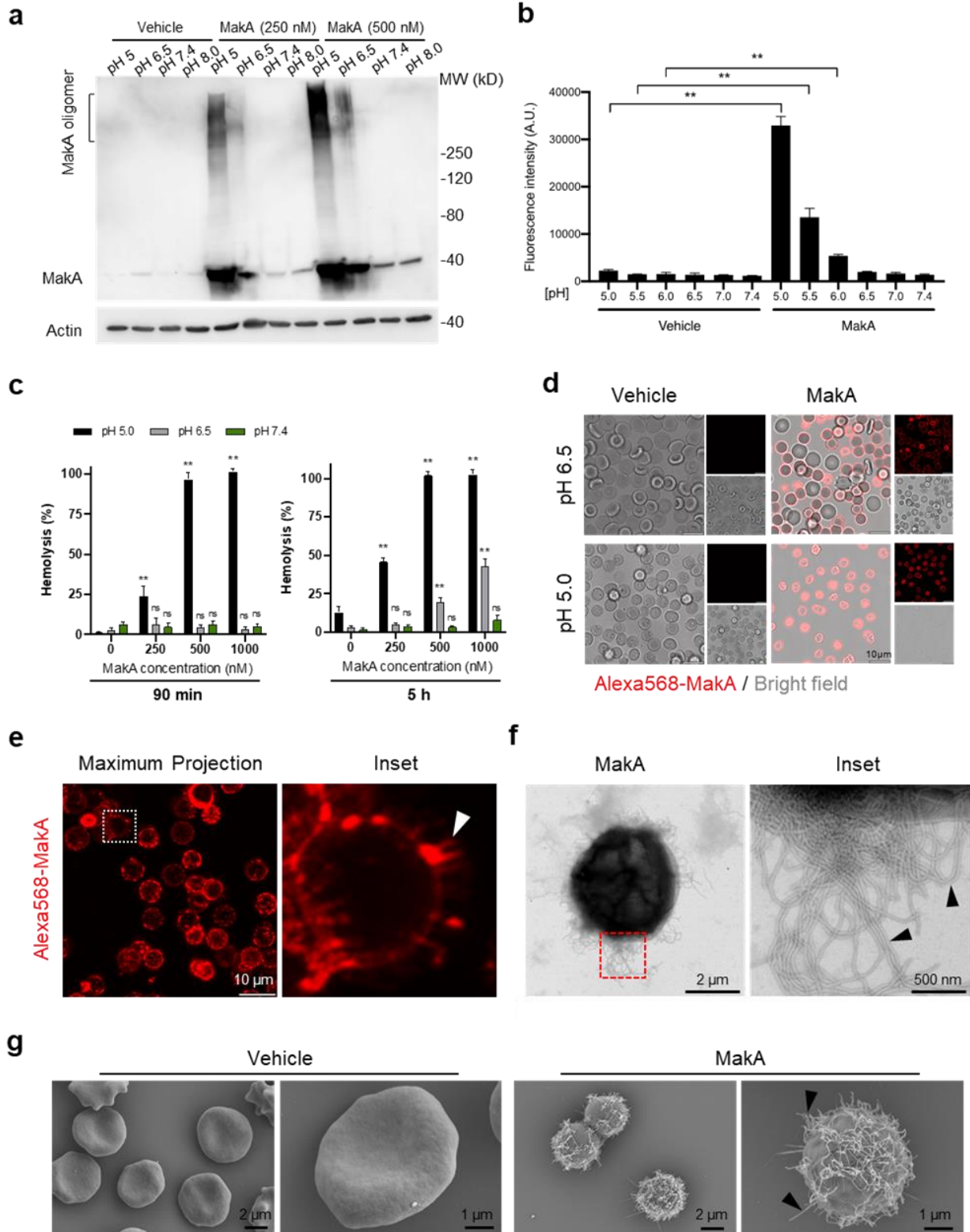
Fig. 2: pH-dependent MakA binding to target cell membranes and induction of tubulation on erythrocytes.

a Western blot analysis of HCT8 cells treated with increasing concentrations of MakA under different pH conditions for 4 h. Data are representative of two independent experiments. Cell-bound MakA was detected with MakA-specific antibodies, and actin was used as a loading control. **b** HCT8 cells were

31

1009   treated with MakA (500 nM, 4 h) under different pH conditions, and cell toxicity was monitored by

1010   assaying the uptake of propidium iodide. Fluorescence values for propidium iodide were recorded by

1011   flow cytometry. Data are representative of three independent experiments; bar graphs show the mean

1012   ± s.d. Significance was determined from biological replicates using a non-parametric t-test. **p≤0.01.

1013   **c** Human erythrocytes suspended in citrate buffer of different pHs were exposed to increasing

1014   concentrations of MakA for 90 min (left panel) and 5 h (right panel). MakA-induced hemolysis of

1015   erythrocytes was normalized against erythrocytes treated with Triton X-100 (0.1%), and data was

1016   expressed as a percentage (%). Data are representative of six readouts from two independent

1017   experiments; bar graphs show mean ± s.d. Significance was determined from biological replicates using

1018   a non-parametric t-test. **p≤0.01, *p≤0.05, or ns = not significant. **d** Human erythrocytes (0.25%) in

1019   phosphate-buffered saline (PBS) were allowed to adhere to the glass surface for 10 h, followed by buffer

1020   exchange to citrate buffer (pH 5.0 or pH 6.5). The erythrocytes were treated with Alexa568-MakA (500

1021   nM, 3 h), and cell-bound MakA was detected by confocal microscopy. Scale bars, 10 μm. **e** The image

1022   shows a maximum z-stack projection of the human erythrocytes treated with Alexa568-MakA (pH 6.5 in

1023   citrate buffer). The white arrowhead in the right panel indicates the accumulation of Alexa568-MakA in

1024   tubular structures at the surface of erythrocytes. Scale bars, 10 μm. **f** Transmission electron microscopy

1025   (TEM) images of erythrocytes treated with vehicle or MakA (500 nM) for 90 min and stained with 1.5%

1026   uranyl acetate solution. Black arrowheads in the enlarged part of the image to the right indicate the

1027   presence of tubular structures present on the surface of the liposome. **g** Scanning electron microscopy

1028   (SEM) images of erythrocytes treated with MakA (500 nM, 90 min) in citrate buffer (pH 6.5).

1029   Representative examples of imaged erythrocytes indicate that the formation of tubular structures

1030   occurred throughout the surface of MakA treated erythrocytes. Scale bars, 2 μm.

1031

1032   **Figure 2; source data**

1033   Uncropped western blot membranes

32
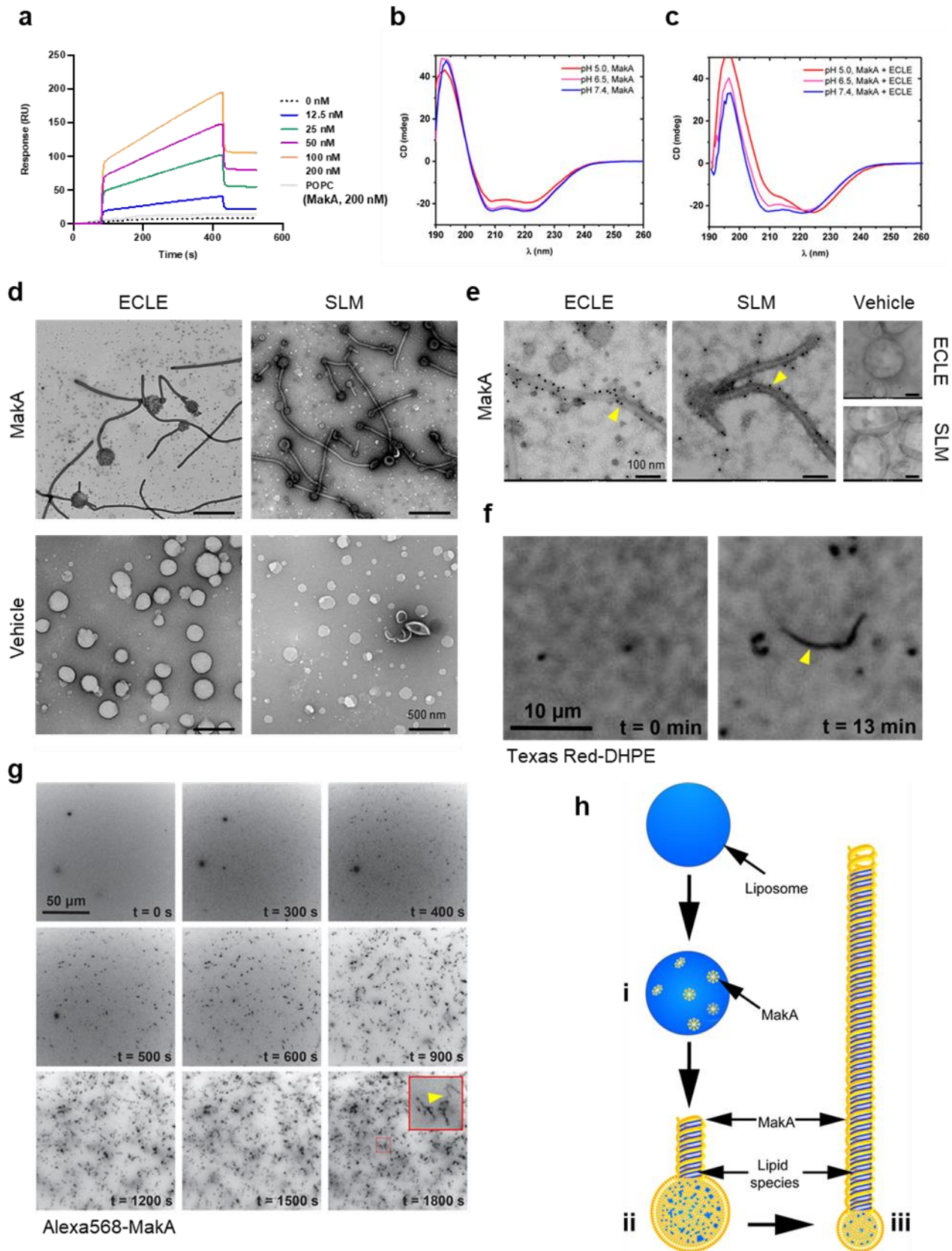
1034

1035

1036 **Fig. 3: pH-dependent formation of protein-lipid tubular structures from MakA interaction with**

1037 **liposomes.**

33

1038　**a** Surface plasmon resonance (SPR) assay showing direct binding of MakA (0 to 200 nM) to ECLE

1039　liposomes (120 mM citrate buffer, pH 6.5). The liposomes were immobilized on an SPR sensor chip L1

1040　(dotted line with 0 nM is buffer control and grey line with immobilized POPC was used as a negative

1041　control). Control flow cell background was subtracted from the experimental cell before final data

1042　processing. The K_D values (49.2 nM) were calculated by using the BioLogic scrubber 2 software. **b** Far-

1043　UV CD spectra of native MakA of MakA bound to ECLE liposomes under different pH condition. CD

1044　spectra were recorded in 5 mM citrate buffer using 3 µM MakA protein. The absorption intensity

1045　measured from the control solution, containing buffer only, was subtracted to account for background

1046　absorption. **d** ECLE or synthetic lipid mixture (SLM) liposomes were treated at pH 6.5 with vehicle (Tris

1047　20 mM) or MakA (3 µM) for 90 min and stained with 1.5% uranyl acetate solution. Images were captured

1048　with transmission electron microscopy (TEM). White arrowheads indicate tubular structures and blue

1049　arrowheads indicate MakA oligomeric structures present in the background of liposomes. Scale bars,

1050　200 nm. **e** The ECLE or SLM liposomes were treated with vehicle (Tris 20 mM) or MakA (3 µM) for 90

1051　min and stained with 1.5% uranyl acetate solution. MakA was detected with anti-MakA antibodies,

1052　followed by immunogold labeling and imaging by TEM. Scale bars, 200 nm. **f** Selected inverted

1053　grayscale images from time-lapse epifluorescence microscopy [Movie 1] obtained after incubating SLBs

1054　(prepared from SLM+TxRed liposomes) with MakA (3 µM) at pH 6.5. The fluctuating tubules (yellow

1055　arrowhead) are visible due to their TxRed-DHPE lipid content. Scale bar, 10 µm. **g** Selected inverted

1056　grayscale images from time-lapse epifluorescence microscopy [Movie 2] obtained after incubating SLBs

1057　(prepared from SLM liposomes) with Alexa568-MakA (3 µM) at pH 6.5. Panels illustrate key steps during

1058　the transformation of SLBs into fluctuating tubules. Arrowhead (yellow) in the inset indicate appearance

1059　of a Alexa568-MakA positive tubular structure. Scale bar, 50 µm. **h** Schematic representation of how

1060　MakA insertion into the liposome can result in formation of a MakA- and lipid-positive tubular structure

1061　under low pH (6.5 or lower) conditions. Upon addition of MakA (yellow) the liposome surface (blue) will

1062　become covered by the protein (steps i and ii) and the MakA oligomerisation initiates formation of a

1063　tube-like structure that gradually appears to deplete the liposome of lipids when the protein-lipid tube

1064　assembly continues to grow in length (step iii).

34
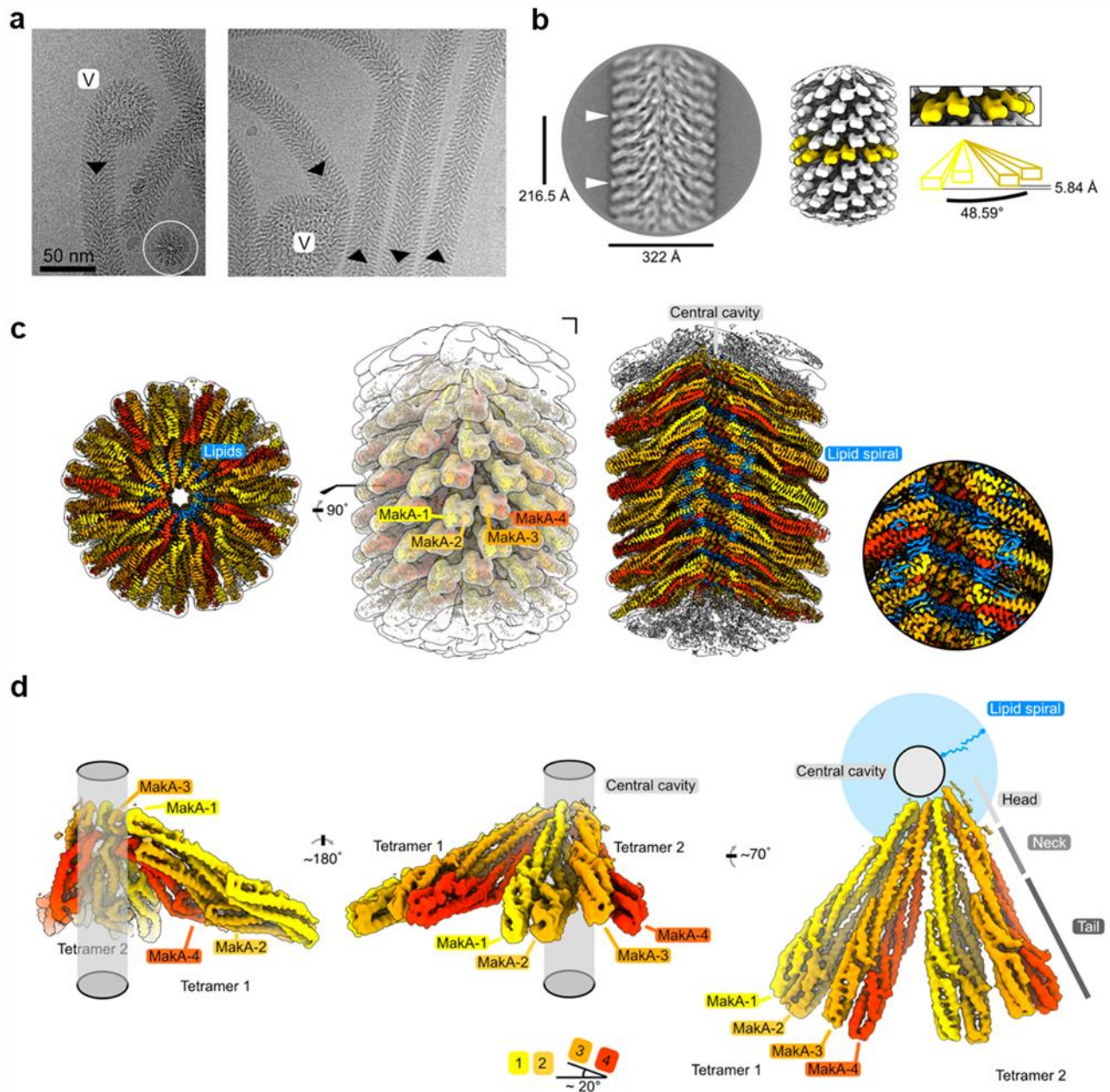
Fig. 4: Cryo-EM structure of the membrane-bound MakA filament.

a Representative cryo-EM micrograph sections showing MakA filaments emerging from or ending in a membranous vesicle (V; vesicle). The black arrows indicate the directionality of the filaments. A top-view of the filamentous tube is visible in the first micrograph within the white circle. **b** A 2D class average with filament diameter indicated below and the repeat distance labeled on the side. An example of a visually repeating element is indicated with white arrows. The right side depicts a low-pass filtered cryo-EM volume with eight repeating subunits colored in gold next to a zoom-in of two blades. A schematic representation of the two repeating units is visualized underneath the zoom-in with a helical twist (48.59º), and rise (5.84 Å) indicated. **c** Overall cryo-EM volume (EMD-13185) and slab views of the MakA filament superimposed onto a semi-transparent, white, 20-Å, low-pass filtered map. The four MakA subunits, belonging to one tetramer, are colored in shades of gold and orange-red and labeled.

35

1078   The different densities between the protein blades belonging to a lipid bilayer is colored in blue. **d**

1079   Rotationally related views of the signal of subtracted and focused-refined cryo-EM volume of two

1080   tetramers (EMD-13185-additional map 1) are shown with a schematic representation of the central

1081   cavity (transparent grey) and the lipid spiral (blue). Common structural elements of the alpha-cytolysin

1082   family protein-fold are indicated in grey (Head, Neck, and Tail). The 20^0-rotation of the tail domain

1083   between two dimers within the asymmetric unit is shown schematically below the central panel.

1084
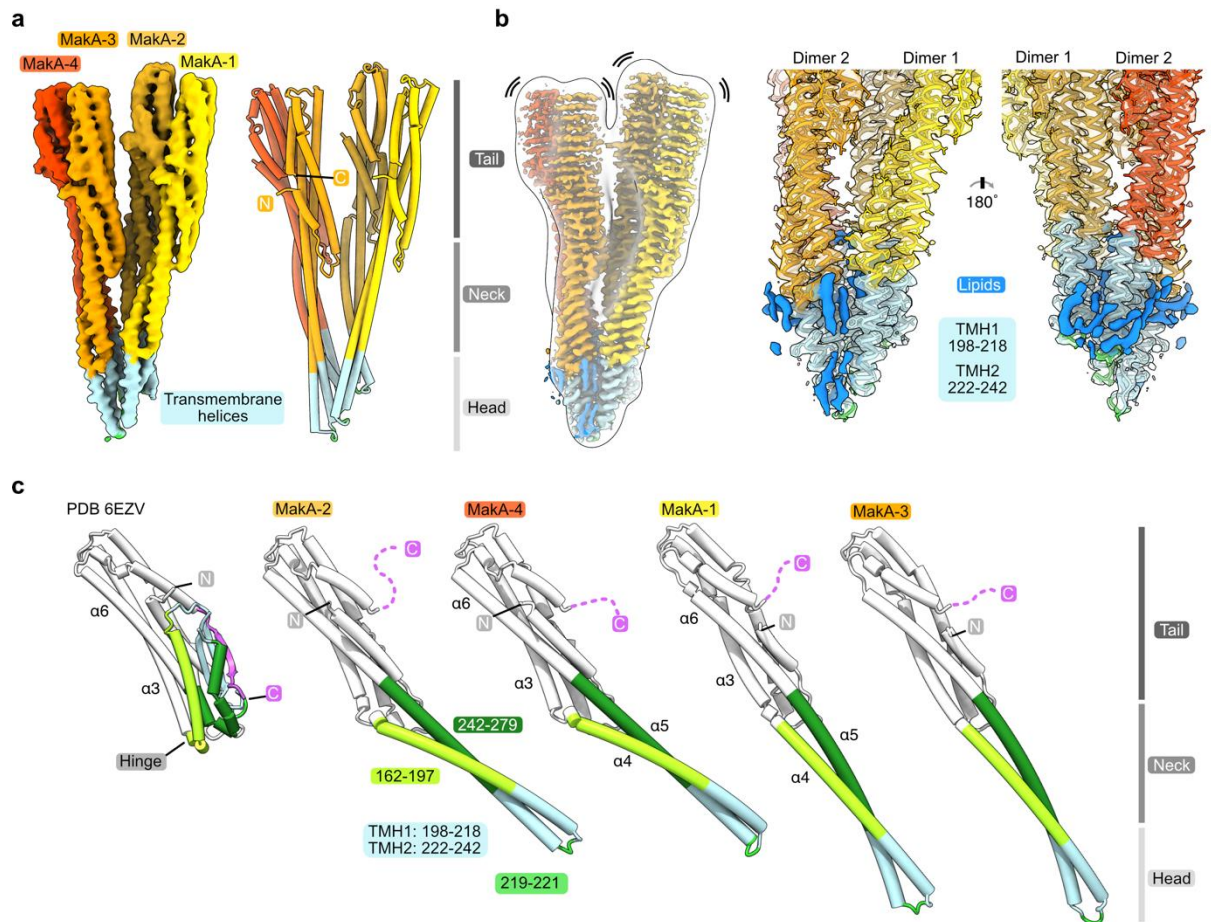
Fig. 5: Conformational plasticity of MakA in the membrane-bound filamentous state.

a The cryo-EM density of a MakA tetramer (EMD-13185-additional map 1) is shown next to a structural model. The individual protein domains (Head, Neck and Tail) and the visible N- and C-terminal are indicated. **b** The cryo-EM density of a MakA tetramer, obtained by helical reconstruction (EMD-13185), is shown in isolation, colored and oriented as the structural model in (**a**). The cryo-EM volume is superimposed with a white, transparent, 20-Å, low-pass filtered volume. Additional density areas in the transmembrane helix (TMH) region, presumably belonging to lipids, are colored in blue. **c** The crystal structure of monomeric MakA (PDB-6EVZ[11]) with retracted neck and head domain is shown next to the four individual subunits of the membrane-bound state of MakA in cartoon representation (PDB-7P3R). All structural models were superimposed based on the tail region (in white) and displayed in the same orientation next to each other with increasing length depicting flexing of the neck and head domain as well as the TMH.

37

1   **Supplementary Information**

2

3   **Protein-lipid interaction at low pH induces oligomerisation of the**
4   **MakA cytotoxin from *Vibrio cholerae***

5

6   Aftab Nadeem[1,2,3]*, Alexandra Berg[1,3,4], Hudson Pace[2,5,7], Athar Alam[2,3,5], Eric Toh[1,2,3],

7   Jörgen Ådén[2,6], Nikola Zlatkov[1,2,3], Si Lhyam Myint[1,2,3], Karina Persson[2,6], Gerhard

8   Gröbner[2,6], Anders Sjöstedt[2,3,5], Marta Bally[2,5,7], Jonas Barandun[1,3,4], Bernt Eric

9   Uhlin[1,2,3]*, Sun Nyunt Wai[1,2,3]*

10

11   [1]Department of Molecular Biology, Umeå University, SE-90187 Umeå, Sweden.
12   [2]Umeå Centre for Microbial Research (UCMR), Umeå University, SE-90187 Umeå, Sweden.
13   [3]The Laboratory for Molecular Infection Medicine Sweden (MIMS), Umeå University, SE-90187
14   Umeå, Sweden.
15   [4]Science for Life Laboratory, Umeå University, Umeå, Sweden
16   [5]Department of Clinical Microbiology, Umeå University, SE-90185, Umeå, Sweden.
17   [6]Department of Chemistry, University of Umeå, SE -901 87, Umeå, Sweden
18   [7]Wallenberg Centre for Molecular Medicine, Umeå University, SE-90185, Umeå, Sweden.
19
20

21   * Corresponding authors: Aftab Nadeem, e-mail: aftab.nadeem@umu.se
22   Bernt Eric Uhlin, e-mail: bernt.eric.uhlin@umu.se
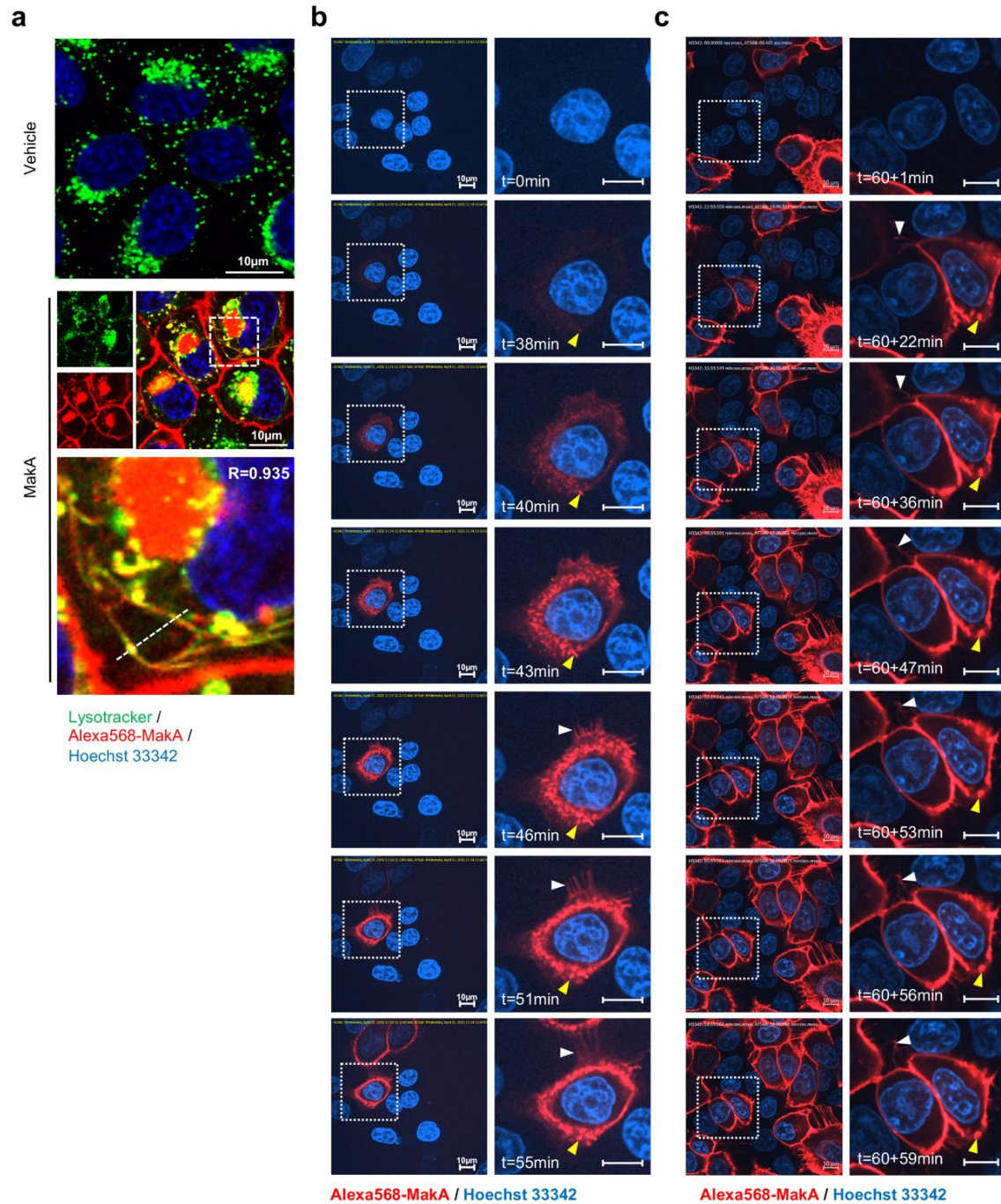23   Sun Nyunt Wai, e-mail: sun.nyunt.wai@umu.se

24

25

26   Short title: pH-dependent cytolytic MakA activity

Supplementary Fig. 1: MakA binding to the epithelial cell membrane in filipodia rich structures.

a Caco-2 cells treated with vehicle or Alexa568-MakA (250 nM, 18 h) and subsequently counterstained with Lysotracker (green, 500 nM, 30 min). Nuclei were counterstained with Hoechst 33342. Pearson correlation co-efficient was used for the calculation of Alexa568-MakA (red) co-localization with lysotracker (green) along the dotted line. Scale bars, 10 μm. **b-c** Still images of HCT8 cells exposed to Alexa568-MakA (500 nM) at pH 5.0. Yellow arrowheads indicate the accumulation of MakA in filipodia rich structures and white arrowheads indicate the appearance of MakA positive tubular structures. Nuclei were counterstained with Hoechst 33342. Scale bars, 10 μm. Images in (a) were acquired for a

2

36 time limit of 55 min immediately after Alexa568-MakA administration, while images in (b) were acquired

37 for 59 extra minutes, 60 min (Total time = 119 min) after Alexa568-MakA administration.
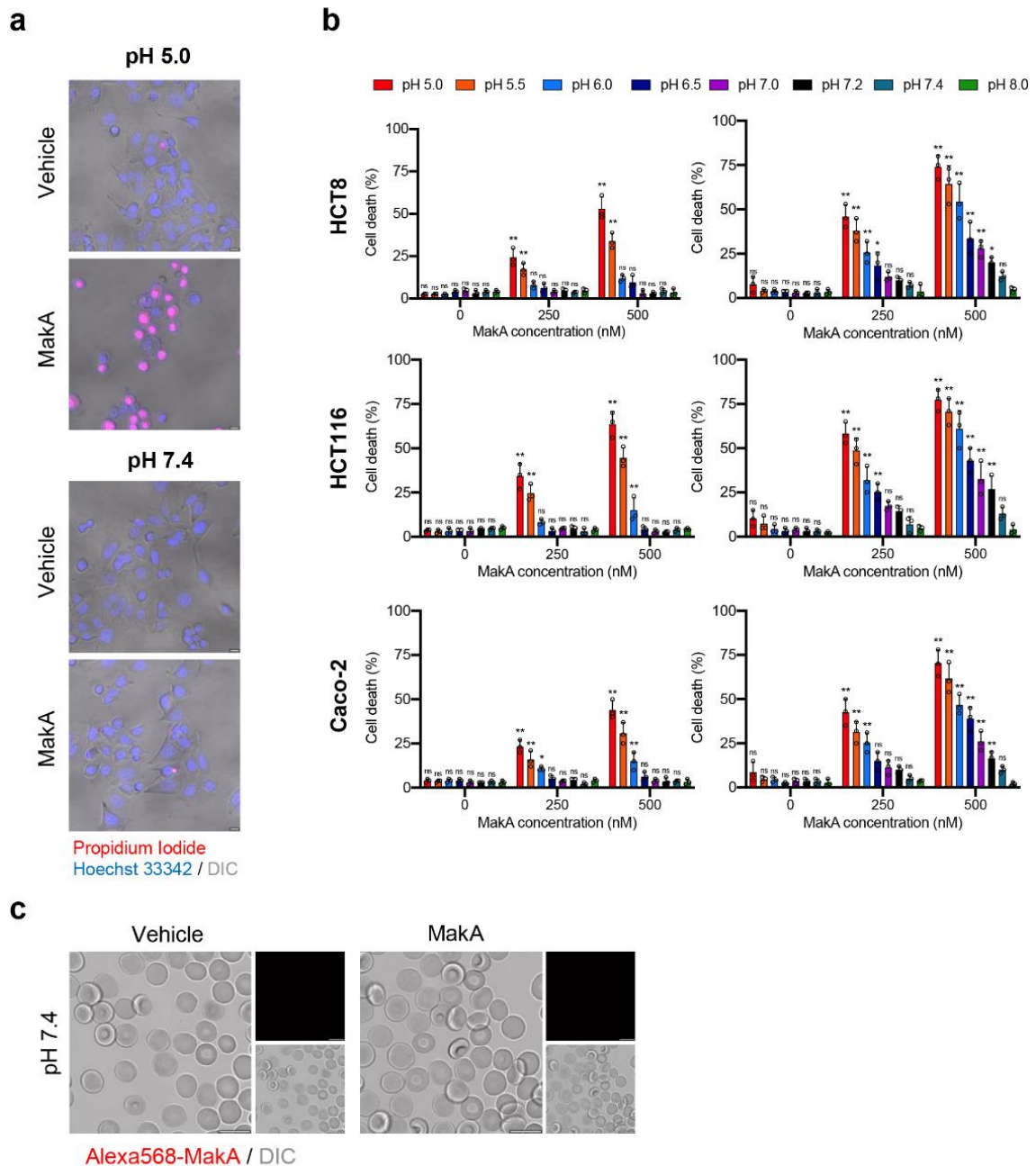
Supplementary Fig. 2: pH-dependent cytotoxicity of MakA in target cells.

a MakA caused pH-dependent permeability of HCT8 cells as determined by cellular uptake of propidium iodide. The uptake of propidium iodide (red) was assessed by confocal microscopy. Scale bars, 10 μm.

b MakA induced death of Caco-2, HCT116 and HCT8 cells under different pH conditions. Epithelial cell viability was assessed using the Trypan blue exclusion method. Data are representative of three independent experiments; bar graphs show mean ± s.d. Significance was determined from biological replicates using two-way analysis of variance (ANOVA) with Tukey's multiple comparisons test. *p≤0.05, **p≤0.01, ns = not significant. **c** Human erythrocytes (0.25 %) in phosphate buffered saline (PBS) were allowed to adhere on the glass surface for 10 h, followed by buffer exchange to citrate buffer (pH 7.4).

48   The erythrocytes were treated with Alexa568-MakA (500 nM, 3 h), and cell-bound MakA was detected

49   by confocal microscopy. Scale bars, 10 μm.

50
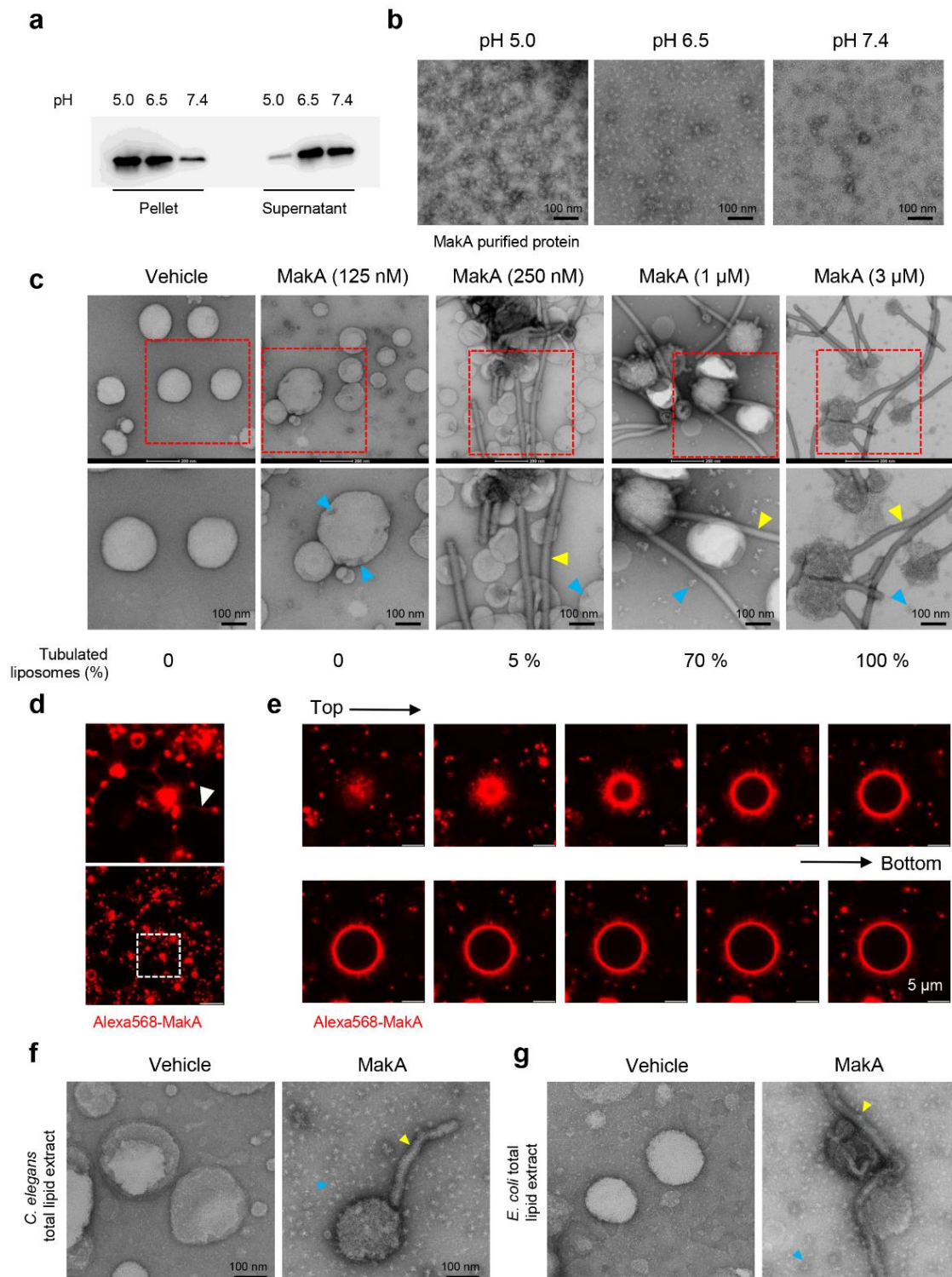
51
52

53   **Supplementary Fig. 3: MakA binding to ECLE liposomes and induction of tubulation in a pH-**

54   **dependent manner**

5

55   **a** Western blot analysis of ECLE liposome-bound MakA detected with anti-MakA antisera. MakA protein

56   (128 nM) was incubated under different pH conditions with liposomes prepared from epithelial cell lipid

57   extract. S = supernatant and P = pellet. **b** EM micrographs of MakA protein (10 µM) that was incubated

58   at 37°C for 1 h in 120 mM citrate buffer, adjusted to pH 5.0, pH 6.5 and pH 7.4, respectively. The protein

59   samples were spotted on grids and stained with 1.5 % uranyl acetate solution. Images were captured

60   with transmission electron microscopy (TEM). MakA appeared as oligomers of varying size under the

61   different pH conditions. Scale bars, 100 nm. **c** ECLE liposomes were treated with increasing

62   concentration of MakA for 90 min and stained with a 1.5 % uranyl acetate solution. Images were

63   captured with TEM. Yellow arrowheads indicate tubular structures, blue arrowheads indicate the

64   formation of MakA oligomeric structures present nearby or on liposomes. Scale bars, 200 nm and 100

65   nm. A quantification (%) of liposomes with tubular structures is shown below the micrographs. **d-e** ECLE

66   liposomes were treated with Alexa568-MakA (1 µM, 90 min, pH 6.5). Liposome-bound MakA across the

67   tubular structure (arrowhead, white) was detected by confocal microscopy. Scale bars, 5 µm. Selected

68   images from z-stack projection of liposome-bound Alexa568-MakA are shown (Top = topmost section,

69   Bottom = section close to the coverslip). The fraction of large vesicles was less than 1% in the reaction

70   mixture. **f-g** Liposomes prepared from *C. elegans* or *E. coli* total lipid extracts were treated with MakA

71   (3 µM, 90 min) at pH 6.5. Yellow arrowheads indicate MakA induced tubular structures and blue

72   arrowheads indicate MakA oligomers. Scale bars, 200 nm and 100 nm.
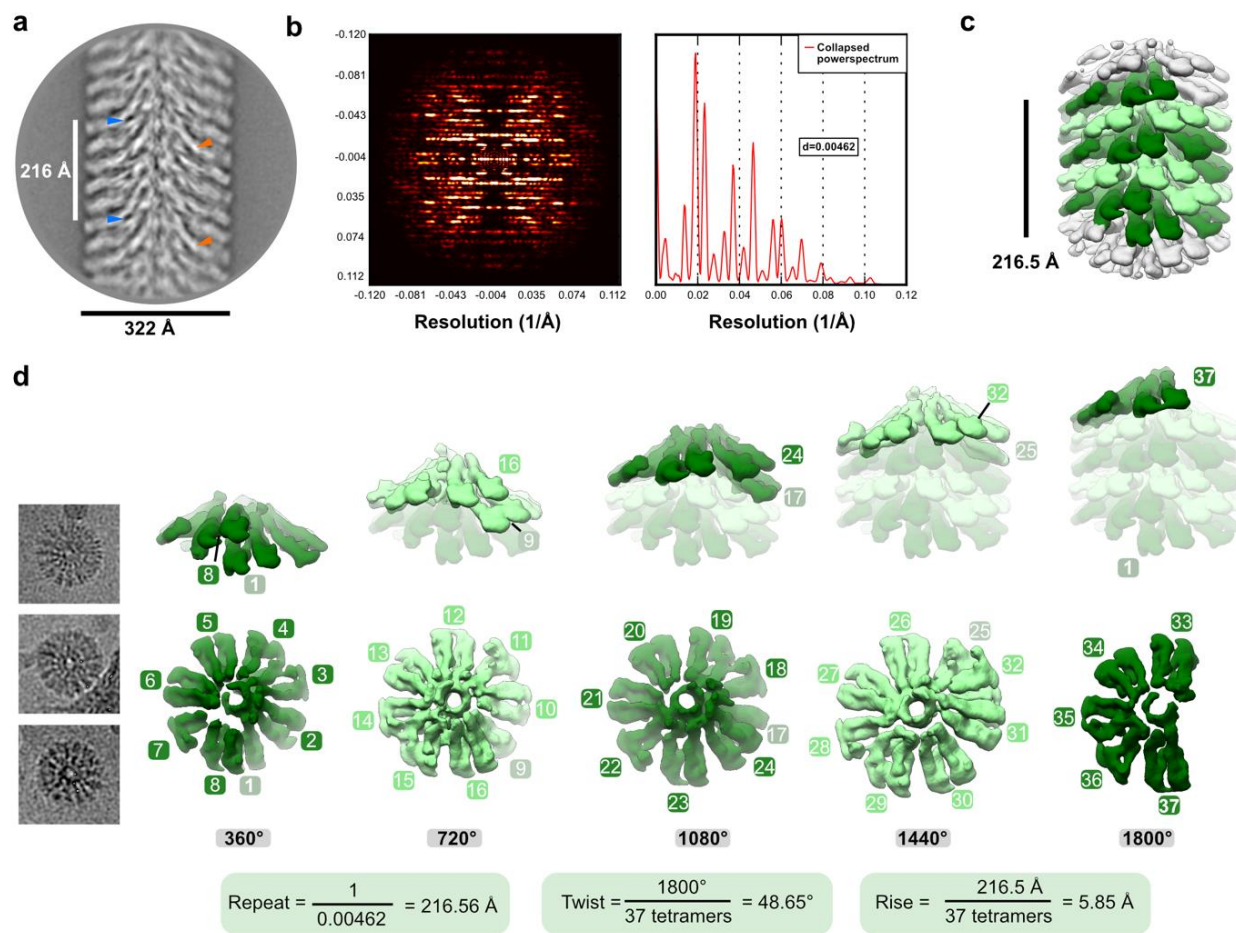
73

74

75
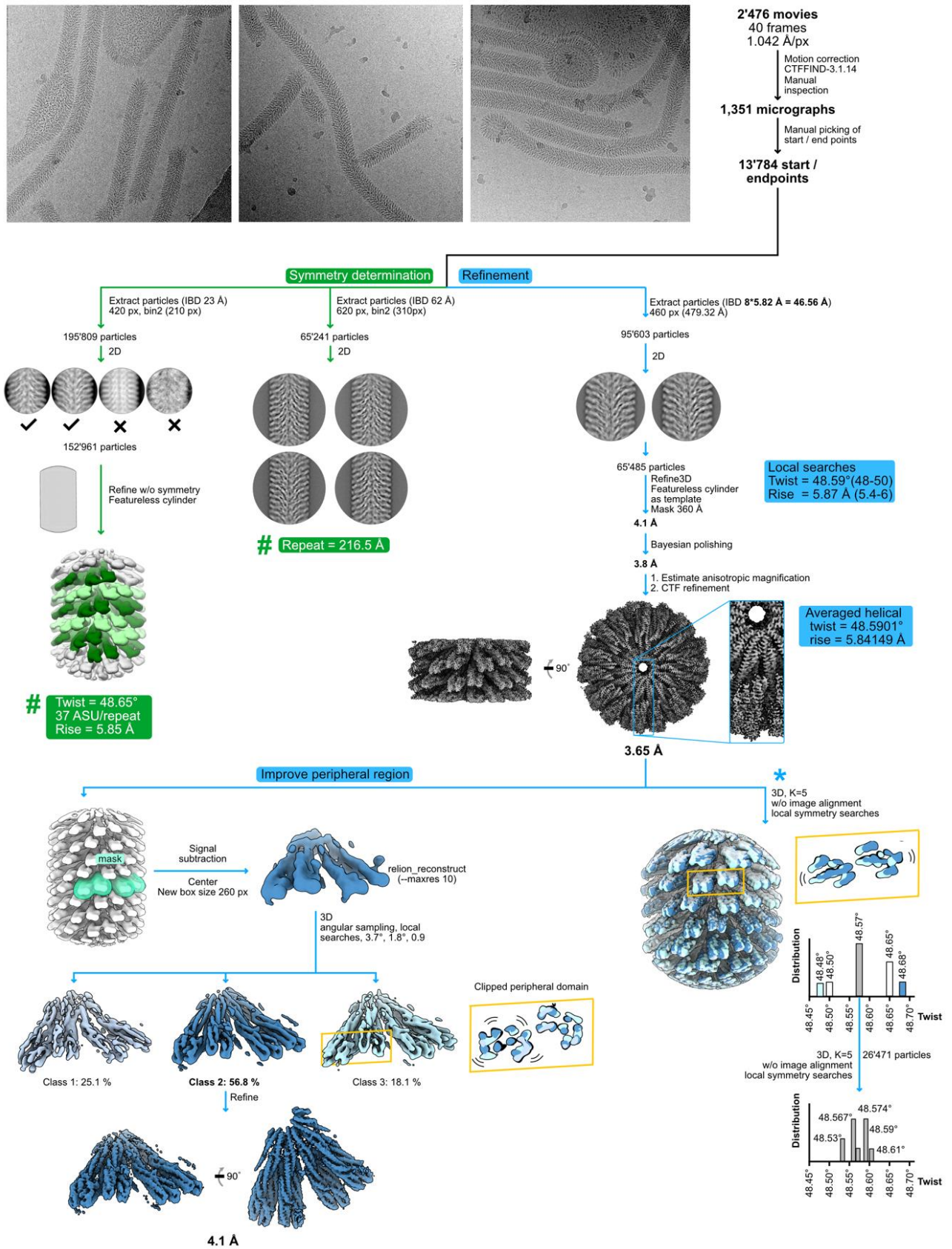
**Supplementary Fig. 4: Cryo-EM processing scheme**

77   Three representative micrographs are shown next to a schematic sorting and data processing tree. The

78   green branch of the tree indicates steps performed to obtain symmetry parameters of the filament, while

79   the blue branch outlines high-resolution refinement. Within the green branch, the (#) refers to

80   (Supplementary Fig. 5), which details how the listed symmetry parameters were obtained. The branch

81   depicted with a (*) describes two consecutive 3D classification experiments, performed without image

82   alignment but with local searches of helical symmetry, to analyze the presence of continuous motion or

83   concrete states in the filament.

84

$$Repeat = \frac{1}{0.00462} = 216.56 \text{ Å}$$

$$Twist = \frac{1800°}{37 \text{ tetramers}} = 48.65°$$

$$Rise = \frac{216.5 \text{ Å}}{37 \text{ tetramers}} = 5.85 \text{ Å}$$

Supplementary Fig. 5: Helical symmetry determination of the MakA-filament.

a A representative 2D class average, obtained from segments extracted with a large box size of 646 Å using RELION-3.1 (ref. [1]), is shown. Visual analysis and measurements of the distance between repetitive elements in the 2D class averages (examples indicated with blue or orange arrows) suggest a repeat distance of 216 Å. **b** Enhanced (left), and corresponding collapsed power spectrum (right, red curve), obtained from the class average shown in (a) using SPRING-0.86 (ref. [2]), confirms a repeat distance of ~216 Å. **c** A volume, obtained by refining well-defined class averages showing high resolution features without symmetry in RELION-3.1, is shown 20 Å low-pass filtered with one repeat colored in shades of green. **d** Three filament top views, cut out from micrographs, are shown next to a dissection of the volume depicted in (c). The five turns, constituting one repeat, are demonstrated individually, starting with the first (left) and ending with the last turn (right). The lower row visualizes a top view of each turn with individual repetitive segments numbered. The top row shows the corresponding turns in a side view in solid colors, superimposed with a transparent filament. The resulting calculated symmetry parameters are shown below the dissected repeat.

9

102
103
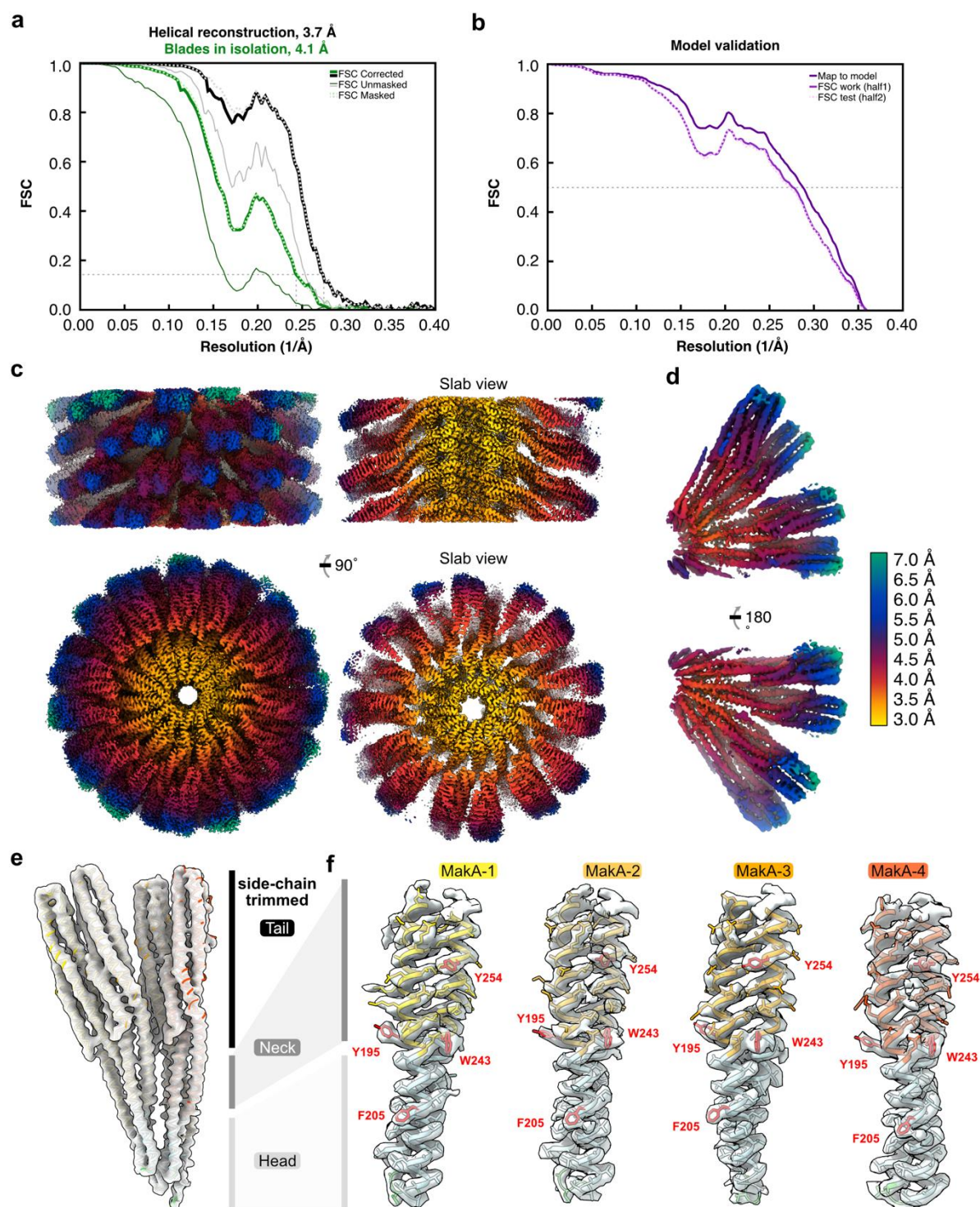
Supplementary Fig. 6: Global and local resolution estimation, model validation, and density fit.

a The Fourier Shell Correlation (FSC) curves, obtained from RELION-3.1 (ref. [1]), are shown for the helical reconstruction (EMD-13185) and the two tetramers refined in isolation (EMD-13185-additional map 1). An FSC value of 0.143 is indicated with a thin dashed line. **b** Cross-validation of the final refined model and map (dark-purple line) and a modified "scrambled" model (random displacement of all atoms by 0.5 Å), refined against 50% of the data, compared against half map 1 (solid purple line) or the independent half map 2 (dashed light-purple line). A thin dashed line indicates an FSC value of 0.5. **c**

111   Two 90-degree related views of the helical reconstruction are shown from the side and the top, next to

112   two slab views. **d** Two 180-degree related views of the two tetramers refined in isolation are visualized.

113   The cryo-EM densities in (c,d) are colored according to local resolution, which was estimated using

114   RELION-3.1 and visualized in UCSF ChimeraX (ref. [3]). **e,f** The overall model to density fit between the

115   final refined model (PDB-7P3R) and (e) the 4.1 Å cryo-EM map (EMD-13185-additional map 1) or (f)

116   sections of the peripheral Head and Neck domains of the 3.7 Å map (EMD-13185). The individual copies

117   of MakA are colored in shades of red and orange with the transmembrane domains highlighted blue.

118   Selected bulky residues are indicated and labeled with amino acid code and residue number in red.

119

120 **Supplementary Table 1. Cryo-EM data collection, refinement and model statistics.**

121

122

	MakA helical reconstruction	MakA, tetramers in isolation
	EMD-13185	EMD-13185-additional map 1
	PDB-7P3R	
Data collection and processing		
Voltage (kV)	300	300
Pixel Size (Å)	1.042	1.042
Electron exposure (e-/Å^2)	43	43
Defocus range (μm)	0.7 – 2.5	0.7 – 2.5
Frames	40	40
Symmetry imposed		C1
Helical twist (˚)	48.59	-
Helical rise (Å)	5.84	-
Initial particle images	95'603	95'603
Final particle images	65'485	37'876
Resolution (Å)	3.7	4.1
FSC threshold	0.143	0.143
Map sharpening B-Factor (Å^2)	-99.9	-117
Refinement		
Initial model used	6EZV	6EZV
Model composition		
Non hydrogen Atoms	7'738	
Protein residues	1'338	
R.m.s deviations		
Bond length (Å)	0.0069	
Angles (°)	1.17	
Validation		
MolProbity score	1.08	
Clashscore	1.88	
Poor rotamers (%)	0.28	
Ramachandran		
Favored (%)	97.29	
Allowed (%)	2.71	
Outliers (%)	0.00	

123
124
125

126
References

128   1.   Zivanov J, *et al.* New tools for automated high-resolution cryo-EM structure
129   determination in RELION-3. *Elife* **7**, (2018).

131   2.   Desfosses A, Ciuffa R, Gutsche I, Sachse C. SPRING - an image processing package
132   for single-particle based helical reconstruction from electron cryomicrographs. *J*
133   *Struct Biol* **185**, 15-26 (2014).

135   3.   Goddard TD, *et al.* UCSF ChimeraX: Meeting modern challenges in visualization and
136   analysis. *Protein Sci* **27**, 14-25 (2018).